UC Riverside

UC Riverside Previously Published Works

Title

Epistatic interactions between NMD and TRP53 control progenitor cell maintenance and brain size

Permalink

https://escholarship.org/uc/item/9742k8ch

Journal

Neuron, 112(13)

ISSN

0896-6273

Authors

Lin, Lin

Zhao, Jingrong

Kubota, Naoto

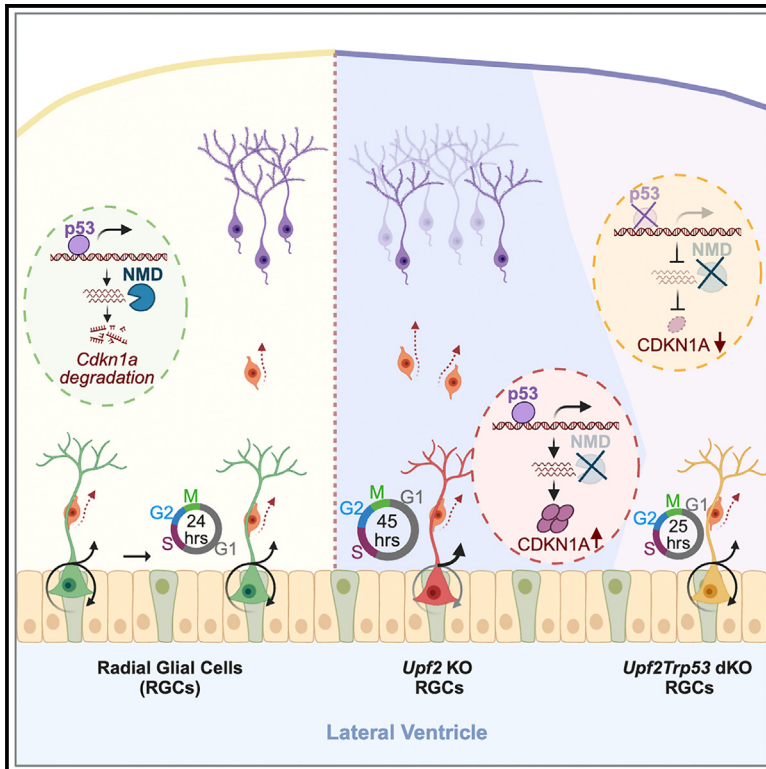et al.

Publication Date

2024-07-01

DOI

10.1016/j.neuron.2024.04.006

Peer reviewed

Epistatic interactions between NMD and TRP53 control progenitor cell maintenance and brain size

Graphical abstract

Authors

Lin Lin, Jingrong Zhao,
Naoto Kubota, ..., Chun-Wei Chen,
Liang Chen, Sika Zheng

Correspondence

sikaz@ucr.edu

In brief

Lin et al. discover that NMD counteracts the TRP53 pathway to regulate neuronal progenitors' cell-cycle progression *in vitro* and *in vivo*. These findings demonstrate that through the selective degradation of TRP53 targets, such as *Cdkn1a*, continuous NMD activity is needed to control progenitor cell cycle and brain size during development.

Highlights

- *Upf2*KO in neural progenitors prolongs cell cycle and causes microcephaly

- *Trp53* depletion rescues *Upf2KO* progenitor cell cycle and microcephaly

- Most NMD targets have a marginal contribution to the cell-cycle defect

- NMD degrades TRP53 target, *Cdkn1a*, to maintain progenitor cell pools

CellPress

Neuron

CellPress

Article

Epistatic interactions between NMD and TRP53 control progenitor cell maintenance and brain size

Lin Lin,[1,2,9] Jingrong Zhao,[1,2,9] Naoto Kubota,[1,2] Zhelin Li,[1] Yi-Li Lam,[1,2] Lauren P. Nguyen,[3] Lu Yang,[4]
Sheela P. Pokharel,[4] Steven M. Blue,[6,7] Brian A. Yee,[6,7] Renee Chen,[4] Gene W. Yeo,[6,7] Chun-Wei Chen,[4,5] Liang Chen,[8]
and Sika Zheng[1,2,3,10,*]
[1]Division of Biomedical Sciences, School of Medicine, University of California, Riverside, Riverside, CA 92521, USA
[2]Center for RNA Biology and Medicine, University of California, Riverside, Riverside, CA 92521, USA
[3]Interdepartmental Neuroscience Program, University of California, Riverside, Riverside, CA 92521, USA
[4]Department of Systems Biology, Beckman Research Institute, City of Hope, Duarte, CA, USA
[5]City of Hope Comprehensive Cancer Center, Duarte, CA, USA
[6]Department of Cellular and Molecular Medicine, University of California, San Diego, La Jolla, CA, USA
[7]Institute for Genomic Medicine, University of California, San Diego, La Jolla, CA, USA
[8]Department of Quantitative and Computational Biology, University of Southern California, Los Angeles, CA 90089, USA
[9]These authors contributed equally
[10]Lead contact
*Correspondence: sikaz@ucr.edu
https://doi.org/10.1016/j.neuron.2024.04.006

SUMMARY

Mutations in human nonsense-mediated mRNA decay (NMD) factors are enriched in neurodevelopmental disorders. We show that deletion of key NMD factor *Upf2* in mouse embryonic neural progenitor cells causes perinatal microcephaly but deletion in immature neurons does not, indicating NMD's critical roles in progenitors. *Upf2* knockout (KO) prolongs the cell cycle of radial glia progenitor cells, promotes their transition into intermediate progenitors, and leads to reduced upper-layer neurons. CRISPRi screening identified *Trp53* knockdown rescuing *Upf2*KO progenitors without globally reversing NMD inhibition, implying marginal contributions of most NMD targets to the cell cycle defect. Integrated functional genomics shows that NMD degrades selective TRP53 downstream targets, including *Cdkn1a*, which, without NMD suppression, slow the cell cycle. *Trp53*KO restores the progenitor cell pool and rescues the microcephaly of *Upf2*KO mice. Therefore, one physiological role of NMD in the developing brain is to degrade selective TRP53 targets to control progenitor cell cycle and brain size.

INTRODUCTION

A cell's transcriptomic identity is shaped as much by RNA decay as by transcription. Little is known about the contribution of regulated mRNA decay to neurogenesis. Nonsense-mediated mRNA decay (NMD) has emerged as an essential and understudied post-transcriptional regulatory mechanism. Originally conceptualized as a surveillance pathway, NMD degrades nonsense mRNAs harboring premature termination codons (PTCs) that result from DNA mutations or aberrant pre-mRNA processing. Recent studies show that NMD factors can target normal physiological mRNAs without PTCs.[1,2] Therefore, in addition to ensuring transcript quality, NMD factors modulate mRNA stability to fine-tune transcript abundance.

Genes involved in the biochemical regulation of NMD are implicated in neurodevelopmental diseases. The mammalian core NMD machinery includes UPF1, UPF2, UPF3A, UPF3B, SMG1, SMG5, SMG6, SMG7, etc.[3–5] In the current working model, UPF1 assembles with UPF2, UPF3A/B, and target mRNA to form a complex, which recruits endonuclease SMG6 and exonucleases to degrade mRNAs.[6–10] Copy-number variants of *Upf2*, *Upf3a*, and *Smg6*, as well as *Upf3b* null mutations, are significantly enriched in patients with autism and intellectual disability.[11–14] Therefore, NMD factors play an important role in brain development.

How NMD influences brain development remains elusive. *In vitro* neural stem cell (NSC) differentiation models suggested NMD's involvement in neurogenesis but arrived at different conclusions about NMD's functional roles. *Upf3b* knockdown in NSC was first reported to increase proliferation and reduce differentiation *in vitro*,[15] but a separate study found that knockdown of *Upf3b* or *Upf1* promoted NSC differentiation.[16] Subsequent studies showed that NSC expressing defective *Upf3b* or depleted *Upf3b* differentiated poorly.[17,18] These differences may be due to the variability of *in vitro* systems. In light of the complexity and dynamics of neural progenitors and lineage progression during brain development, the role of NMD in neurogenesis needs to be characterized *in vivo* using intact animals.

Although transcriptional controls of progenitor cell fate have been extensively studied, little is known about the contribution of regulated mRNA decay. Apical radial glial cells (RGCs) are the primary cortical progenitor cells residing within the ventricular zone (VZ) of the developing neocortex.[19,20] During early corticogenesis, a thin layer of neural epithelial stem cells undergoes proliferative mitosis to expand the progenitor cell pool and generate RGCs. Many RGCs switch to differentiative divisions producing a self-renewing RGC and a lineage-restricted intermediate progenitor cell (IPC).[21,22] Murine IPCs are the major transit-amplifying progenitors localized in the subventricular zone (SVZ) and often produce two immature neurons.[19,23,24] Virtually all RGCs and IPCs are positive for transcription factors PAX6 and TBR2, respectively.[25,26]

The underlying transcriptomic changes for lineage transitions (e.g., RGC-to-IPC) have become more accessible,[27–34] but their regulation remains largely unknown. Transcriptional potency, indicated by histone modifications (H3K4me3 and H3K27me3) at promoter regions, is not always predictive of gene expression differences associated with neuronal lineage progression.[35] This implies that post-transcriptional mechanisms, e.g., mRNA decay, are essential to finetuning cell-type-specific transcriptomes and regulating neuronal lineage transitions.

In addition to lineage progression, regulation of progenitor cell division is critical to brain development. Cell-cycle analyses, clonal lineage tracing, and mathematical modeling show that most neural progenitors undergo a defined number of cell cycles during neurogenesis.[36–38] The finite developmental time window implies a tight regulation of cell cycle length in RGCs to ensure normal development, as a longer cell cycle leads to fewer divisions and fewer total neuronal outputs (aka, microcephaly). Whether and how the neural progenitor cell cycle is influenced by mRNA decay pathways remains to be determined.

In this study, we thoroughly characterized the role of NMD for progenitor cell maintenance and differentiation during *in vivo* neurogenesis. Because germline deletions of *Upf1*, *Upf2*, *Upf3a, Smg1*, and *Smg6* are lethal between E7.5 and E12.5 in mice,[39–42] we generated an *Upf2* conditional knockout (cKO) allele in the mouse developing brain. UPF1 has molecular activities other than functioning in NMD, and mammalian UPF3 has two homologs, UPF3A and UPF3B.[6] Therefore, *Upf2*cKO is a genuine model to study the genetic necessity for NMD.

RESULTS

Upf2 conditional KO in neural progenitors leads to microcephaly in mice
Upf2 is highly expressed in the brain compared with other tissues (Figure S1A). Its expression is even higher in embryonic brains than in postnatal and adult brains (Figures S1B and S1C). We also found that UPF2 expression is comparable in primary neural progenitor cells (NPCs) and primary immature neurons (Figures S1D and S1E). The expression pattern suggests that *Upf2* plays an important role in early brain development.

To study *Upf2* function in cortical neurogenesis, we bred the *Upf2*fl/fl mouse line with multiple widely used neural-restricted Cre lines to generate the *Upf2*cKO mouse models (Figure 1A).

First, we bred *Upf2*fl/+ Emx1-Cre mice with *Upf2*fl/fl mice to generate *Upf2*fl/fl Emx1-Cre (Emx1-*Upf2*cKO) mice that removed *Upf2* from the forebrain NPCs.[43,44] Although the Emx1-Cre line also directs Cre recombinase activity to glial progenitor cells of the pallium,[43] during embryonic neurogenesis, these forebrain NPCs (also known as RGCs *in vivo*) mainly give rise to cortical excitatory neurons. The Emx1-*Upf2*cKO mice showed a substantial reduction in cortex size and thickness at birth compared with their littermate controls with shrunk ventricles (Figures 1B–1E). By contrast, the striatum area appeared normal (Figures 1C and 1F). We quantified the absolute number of NeuN+ neurons per 200-μm-width bin and found a significant decrease in P0 Emx1-*Upf2*cKO cortices (Figures 1G and 1H). Therefore, the microcephaly is due to fewer neurons. Consistent with the observation that UPF2 depletion in the Emx1-Cre line affects the lineage of excitatory neurons, the decreased relative expression in NEUROD2 and increased relative expression in GAD67 were observed in the mutant cortices, especially at E17.5, indicating a reduction in excitatory neurons and consequently an increase in the relative proportion of inhibitory neurons (Figures S2A–S2D). The brain weight of Emx1-*Upf2*cKO mice at birth decreased significantly, and the animals died within 6 weeks after birth (Figures 1I and S2E), revealing an indispensable role for UPF2 in neural development and mammalian organism survival.

We also deleted *Upf2* from newly generated postmitotic cortical neurons using Nex-Cre mice (Figure 1A). Similar to the Emx1 line, target genes are deleted in cortical excitatory neurons, but different from the Emx1 line, NPCs are spared in the Nex-Cre background.[45] We confirmed that Cre expression was exclusive to the cortical plates and undetectable in the PAX6+ progenitor cell region (Figure S2F). Interestingly, Nex-*Upf2*cKO exhibited comparable brain weight, cortical thickness, ventricle, and striatum sizes with no microcephaly (Figures 1B, 1I, and S2G–S2J). At P0, the UPF2 protein was similarly depleted in these two genotypes and therefore did not account for the phenotypic difference between Emx1-*Upf2*cKO and Nex-*Upf2*cKO (Figures 1J and 1K). Most Nex-*Upf2*cKO mice died within 6 weeks after birth (Figure S2E), suggesting that UPF2 function in postmitotic neurons is also crucial to animal survival.

Based on these observations, neonatal microcephaly in Emx1-*Upf2*cKO arises from defects in cortical NPCs, and UPF2 is required for normal NPC function. To confirm this, we knocked out *Upf2* in a broader range of NPCs using the Nestin-Cre line.[46] *Upf2*fl/fl Nestin-Cre (Nestin-*Upf2*cKO) mice consistently showed an overall reduction of brain size at P0 (Figure 1B).

*Upf2*KO NPCs exhibit slower growth
To study the role of *Upf2* in progenitors, we derived primary cortical NPCs from E14 Nestin-*Upf2*cKO embryos. The neurospheres from E14 Nestin-*Upf2*cKO embryos were substantially smaller compared with those from wild type (WT) (Figure 2A). The CellTiter-Glo Luminescent assay showed that the cell growth of *Upf2*cKO neurospheres from 24 to 120 h after plating was much slower compared with WT (Figure 2B). Because of insufficient cells for further passage (Figures S3A and S3B), we derived *Upf2*fl/fl neurospheres for monolayer cultures, followed

CellPress

Figure 1. *Upf2*cKO in neural progenitors leads to impaired cell growth and microcephaly

(A) Schematic of multiple Cre recombination systems to generate *Upf2* conditional KO mice during brain development.

(B) Images of P0 Emx1-, Nestin-, and Nex-*Upf2*cKO brains with their littermate controls. The dotted lines indicated the forebrains in each *Upf2*cKO.

(C) Images of P0 Emx1-*Upf2*cKO brains and littermate controls with DAPI staining. The white rectangle showed the cortex thickness (scale bars, 500 μm on the left and 50 μm on the right).

(D–F) Quantification of P0 Emx1-*Upf2*cKO cortical thickness (D), ventricle area (E), and striatum area (F) in (C) ($n = 4$; $N = 2$–3 sections per group, two sides per section).

(G) Representative images of NeuN staining in P0 Emx1-*Upf2*cKO cortices and their littermate controls (scale bars, 50 μm).

(H) Quantification of the number of NeuN+ cells per 200 μm bin in (G) ($n = 4$; $N = 2$ images per section and 3–4 sections per sample).

(I) Brain weights of p0 Emx1- and Nex-*Upf2*cKO with their littermate control mice ($n_C = 25$, $n_{Emx1-KO} = 11$, $n_{Nex-KO} = 6$).

(J) Western blotting of UPF2 protein expression in P0 Emx1-*Upf2*cKO and Nex-*Upf2*cKO cortices and their littermate controls.

(K) Quantification of UPF2 expression in (J) ($n_C = 8$, $n_{Emx1-KO} = 6$, $n_{Nex-KO} = 3$).

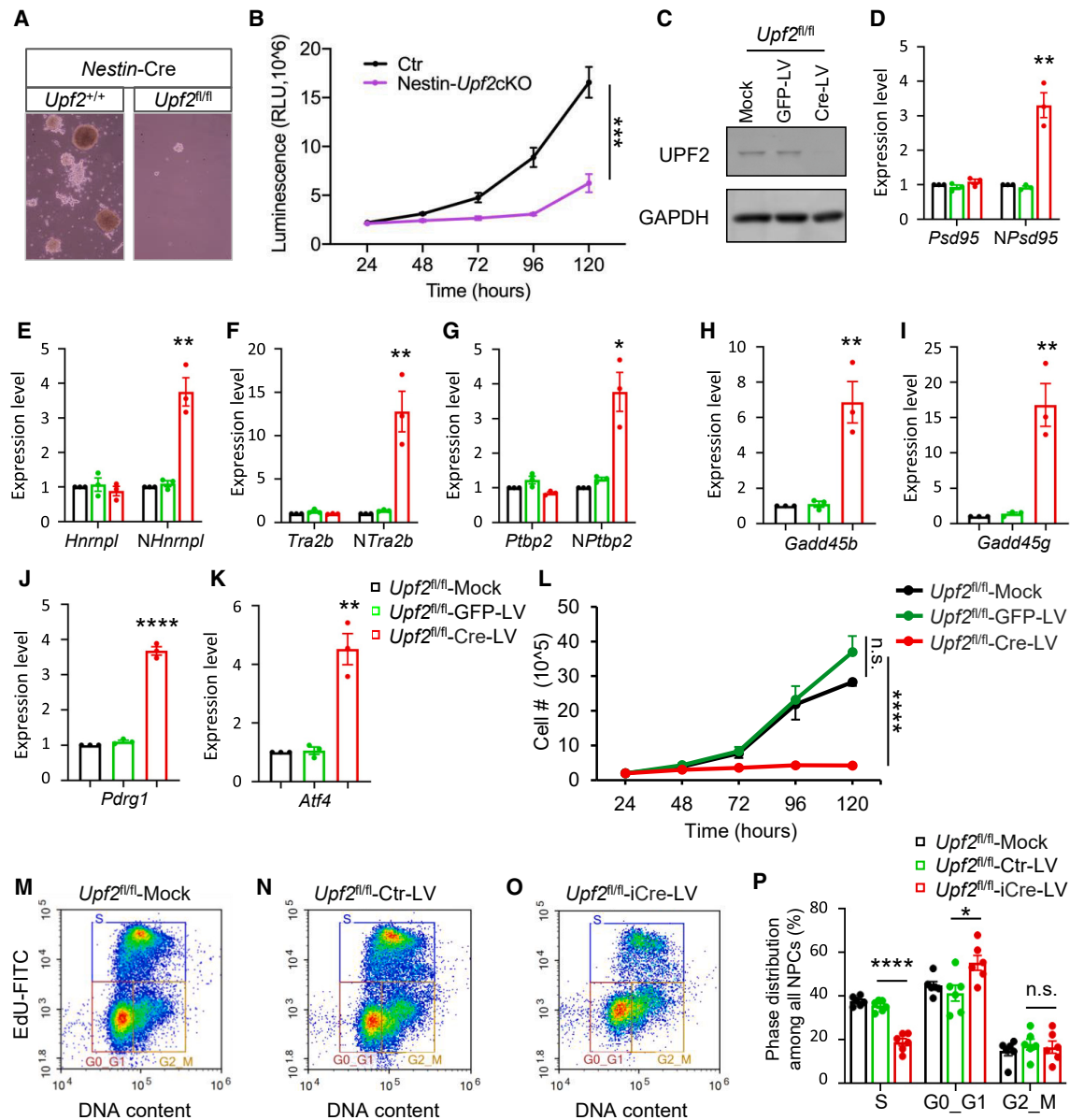See also Figures S1 and S2.

Figure 2. Upf2KO neural progenitor cells exhibit slower growth by inducing cell cycle defects

(A) Nestin-Cre-induced *Upf2*cKO significantly impaired the growth of cortical neurospheres.

(B) CellTiter-Glo luminescent assay performed in E14.5 Nestin-*Upf2*cKO neurospheres and their littermate controls (data are analyzed by two-way ANOVA; *n* = 4).

(C) UPF2 protein in *Upf2*fl/fl NPCs was completely removed after Cre lentivirus infection compared with control groups.

(D–K) The expression level of NMD isoforms and genes showed an upregulation after *Upf2*KO *in vitro*. In *Upf2*KO NPCs, the NMD isoforms (denoted as "N_") of *Psd95* (D), *Hnrnpl* (E), *Tra2b* (F), and *Ptbp2* (G), and other NMD targets such as *Gadd45b* (H), *Gadd45g* (I), *Pdrg1* (J), and *Atf4* (K) showed a significant upregulation (*n* = 3).

(L) *Upf2*fl/fl NPCs with Cre expression had cell growth defects compared with mock and GFP lentivirus control (data are analyzed by two-way ANOVA; *n* = 4).

(M–P) *Upf2*KO NPCs showed cell proliferation defects following EdU labeling. Compared with mock (M) and Ctrl group (N), iCre-infected (O) NPCs had less percentage of S-phase cells after 30 min pulse labeling of 10 μM EdU in (P) (*n* = 6).

See also Figure S3.

by Cre-IRES-GFP lentivirus infection to delete *Upf2* or GFP lentivirus as a control (Figure 2C).

We also verified the *Upf2*KO-induced NMD inhibition by showing that the NMD isoforms of *Psd95*, *Hnrnpl*, *Tra2b*, and *Ptbp2*[47,48] were all substantially upregulated, whereas the cor-

responding non-NMD isoforms barely or modestly changed (Figures 2D–2G). Other reported NMD targets *Gadd45b*, *Gadd45g*, *Pdrg1*, and *Atf4* also significantly increased (Figures 2H–2K).[49–52] These NMD substrates were also significantly upregulated in E17.5 Emx1-*Upf2*cKO mouse cortices

Neuron
Article

CellPress

(Figures S3C–S3J). Upregulation across all the target genes both *in vitro* and *in vivo* shows a clear NMD inhibition.

We found that the *Upf2*KO NPCs grew slower with significantly smaller cell numbers (Figure 2L). The effect was detectable as early as 72 h after lentivirus infection and further amplified at 96 and 120 h. The growth defect could be caused by increased cell death, slowed proliferation, or both. Using the Annexin V/7AAD flow cytometry assay, we found an indiscernible difference in the percentage of dead or apoptotic cells between iCre lentivirus-induced *Upf2*KO and control NPCs (Figures S3K–S3N). Therefore, the deletion of UPF2 did not induce obvious cell death in NPCs. NMD factors were dispensable for embryonic stem cell viability, and their germline mutant mice survived until mid-embryogenesis,[39–42] supporting our result that cell death and cell-cycle arrest are not the default cell fates after NMD inhibition.

The growth defect of *Upf2*KO NPCs was therefore due to slowed division or lengthening of the cell cycle. We used the Click-iT 5-ethynyl-2'-deoxyuridine (EdU) kit to detect the percent of EdU⁺ NPCs after 30 min EdU pulse labeling. Both the Mock and Ctr groups had close to 37% EdU⁺ NPCs (Figures 2M, 2N, and 2P), but the Cre-infected group had only 21.6% (Figures 2O and 2P). By contrast, the G0_G1 phase cells increase by ~14% (Figure 2P). These data confirmed the cell cycle defects in *Upf2*KO NPCs with a defect in the G1-to-S transition.

Cell-cycle defects in *Upf2*KO neural progenitors *in vivo*
To investigate the progenitor cell defects *in vivo*, we examined cortical RGCs in multiple embryonic stages of Emx1-*Upf2*cKO brains and found a gradual reduction in PAX6⁺ RGC numbers over time (Figures 3A and 3B). The *in vivo* reduction in RGC is consistent with the *in vitro* growth defect of NPCs. To examine the cell cycle defect, we injected pregnant mice with bromodeoxyuridine (BrdU) at E17.5 when RGC numbers clearly decreased. After 1.5 h, Emx1-*Upf2*cKO neocortices exhibited a 43% reduction in the number of BrdU⁺ cells (Figures 3C and 3D), consistent with the *in vitro* observation and further suggesting a defect in the G1-to-S transition. We stained cells with Ki67, a marker of cycling cells. The percentage of cycling cells among RGCs (Ki67⁺PAX6⁺/PAX6⁺) exhibited no difference between WT and Emx1-*Upf2*cKO (Figures S4A and S4B). We also performed the cell cycle exit assay by injecting EdU into the pregnant dam at E14.5 and found no difference in the percentage of Ki67⁻EdU⁺/EdU⁺ at E15.5 (Figures 3E and 3F). Therefore, *Upf2*KO RGCs do not prematurely exit the cell cycle, and their lower proliferative potential is due to an increase in cell cycle length.

To quantitatively determine the total cell cycle length (T_C) and the S phase length (T_S) of cortical RGCs *in vivo*, we conducted EdU cumulative labeling (Figure 3G).[53–55] The percentages of EdU⁺ RGCs plotted against cumulative labeling time points gradually increased until reaching a plateau (representing the total proportion of cycling progenitors, or *P*). Because the plateau means all cycling cells are already labeled, the time to reach the plateau (*x*) approximates the time it takes for a cell at the cusp of S/G2 to pass through G2, M, and G1 phases and reenter the S phase (i.e., $T_C - T_S$ or $T_{G2+M+G1}$).

We found that the total proportion of cycling RGCs, or *P*, was nearly 100% in both WT and *Upf2*cKO, consistent with the Ki67

labeling (Figures S4A and S4B). In WT neocortices, it took 14.0 h after the first EdU injection for all cycling RGCs to be labeled by EdU (indicated by the black arrow in Figure 3H); however, this duration lengthened to 26.5 h in UPF2-deficient cortical RGCs (indicated by the red arrow in Figure 3H). Note that this duration time in *Upf2*KO RGCs was inferred by the trend line because the proportion of cycling RGCs had not reached the plateau. We then calculated the values of T_S and T_C to be 9.9 and 23.9 h for WT RGCs, and 18.2 and 44.6 h for *Upf2*KO RGCs (Figure 3I). The values of T_S and T_C for (TBR2⁺PAX6⁻) IPCs were 2.2 and 28.6 h for WT IPCs, and 2.7 and 40.2 h for *Upf2*KO IPCs (Figures S4C and S4D). Taken together, UPF2-deficient cortical progenitors exhibited prolonged cell cycle length at E15.5 *in vivo* and were significantly reduced at E17.5.

RGC-to-IPC lineage defects in *Upf2*cKO mice and the transcriptomic impacts of NMD during RGC lineage transition
Because *Upf2*cKO affected NPC division, we asked whether it also influenced cell lineage progression and found a gradual increase in the percentage of TBR2⁺ IPCs in UPF2-deficient cortices (Figures 4A and 4B). The substantial increases in the ratios of (TBR2⁺%)/(PAX6⁺%) at E15.5 and E17.5 indicated a precocious differentiation from RGCs to IPCs (Figure 4C). To further trace the RGC lineage *in vivo*, we examined the output of GFP⁺ progeny 2 days after delivering GFP-expressing plasmids along the lateral ventricle wall at E14.5 (Figures S4E and S4F). The percentage of PAX6⁺GFP⁺ RGCs among GFP⁺ cells was higher in UPF2-deficient cortices due to the prolonged cell cycle progression. We also observed more TBR2⁺GFP⁺ IPCs in *Upf2*cKO cortices, consistent with the precocious RGC-to-IPC transition (Figures S4F and S4G).

To determine the transcriptomic impacts of NMD on lineage transition *in vivo*, we performed mRNA-seq of neocortices from E13.5 Emx1-*Upf2*cKO and their control littermates (Figure S5A). The E13.5 neocortex is composed of mostly RGCs and IPCs and fewer neurons compared with later developmental stages. Differentially expressed genes (DEGs, fold change [≥2 or ≤0.5], false discovery rate (FDR) ≤ 0.05, and meeting expression thresholds, Figure S5B), either direct or indirect NMD targets are operationally termed NMD-dependent genes. Upregulated genes include *Dll3* and *Insm1*, which reinforces RGC division to produce IPCs.[56–58] Interestingly, neither *Tbr2* (*Eomes*) nor *Neurog2* known to promote the switch were changed (Figure S5C).[59,60] Similarly, some IPC markers increased expression,[56] whereas others did not. Therefore, NMD selectively inhibits some but not all genes linked with the IPC fate.

To understand how NMD inhibition influences RGC lineage transitions (RLTs), we first dissected the transcriptome changes associated with the normal temporal RGC lineage progression: the RGC-to-IPC vs. the early RGC-to-late RGC transitions (Figure 1A). The daughter (late) RGC is intrinsically different from the mother (early) RGC because RGCs gradually change their competence and produce progeny of different fates. We analyzed published single-cell RNA sequencing (scRNA-seq) data from E11, E13, E15, and E17 mouse embryonic cortices.[29] After transcriptomically defining cell clusters of RGCs, IPCs, and neurons based on markers (*Pax6*, *Sox2*; *Tbr2*; *Tbr1*, *Tubb3*, etc.),
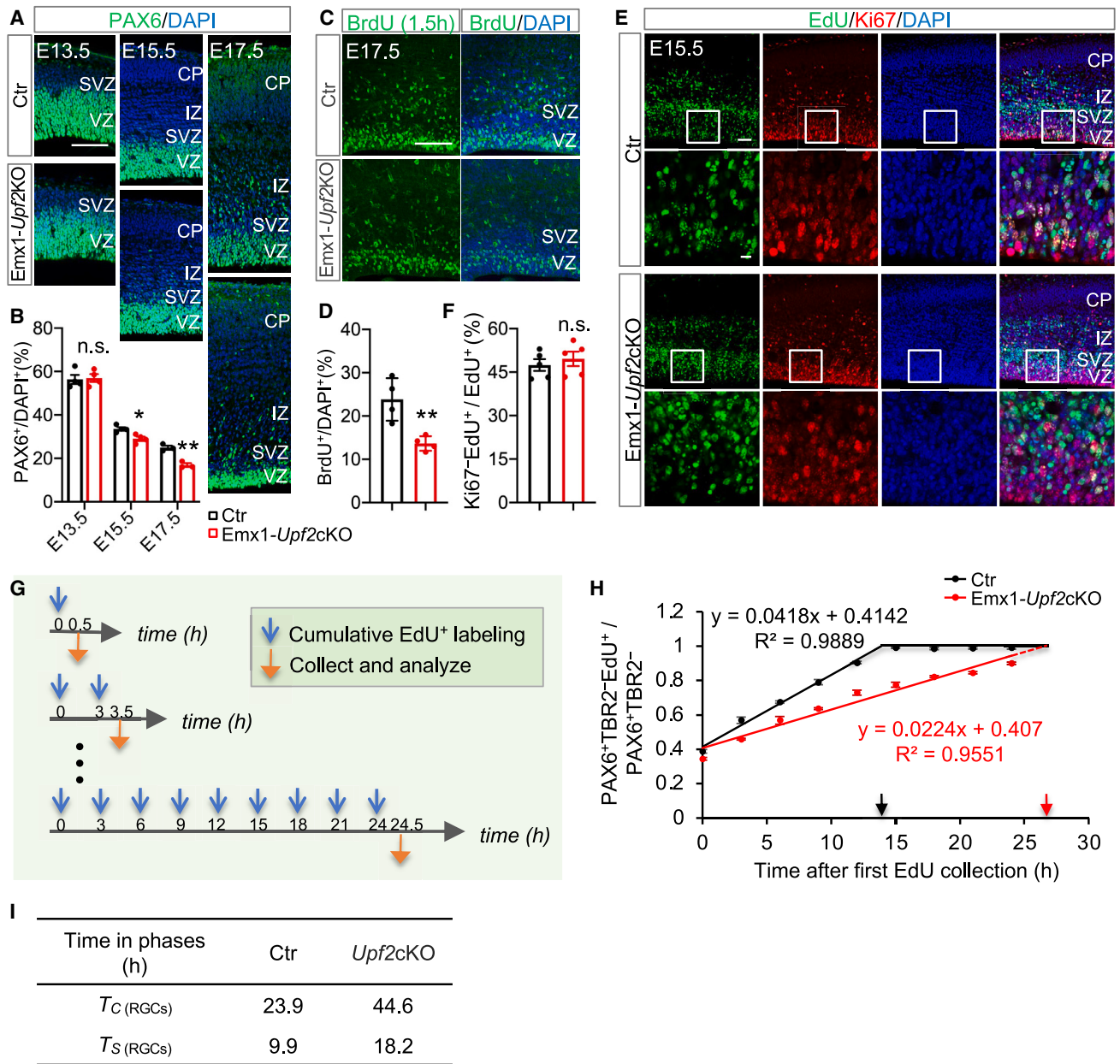
Figure 3. UPF2-deficient RGC exhibited defective proliferation with prolonged cell cycle progression

(A) Immunostaining of PAX6 in E13.5, E15.5, and E17.5 Emx1-*Upf2*cKO cortices and their littermate controls (scale bars, 100 μm).

(B) Quantification of the percentage of PAX6$^+$ cells in (A) ($n = 3–4$; $N = 3–4$ images per section, 2–3 sections per sample).

(C) Immunostaining of BrdU (1.5 h labeling) in E17.5 Emx1-*Upf2*cKO cortices and their littermate controls (scale bars, 100 μm).

(D) Quantification of the percentage of BrdU$^+$ cells in (C) ($n = 4$; $N = 3–4$ images per section, 2–3 sections per sample).

(E) Representative images of EdU (24 h labeling) co-staining with Ki67 in E15.5 Emx1-*Upf2*cKO cortices and their littermate controls (scale bars, 50 μm on the upper and 10 μm on the lower).

(F) Quantification of the cells exiting the cell cycle labeled by Ki67$^-$EdU$^+$ and calculation of the percentage of Ki67$^-$EdU$^+$ in total EdU$^+$ cells in (E) ($n = 5$; $N = 2$ images per section, three sections per sample).

(G) Schematic of cumulative EdU labeling for the experiments in (H) and (I).

(H) Proportion of EdU-labeled RGCs (EdU$^+$PAX6$^+$ TBR2$^-$) after cumulative EdU labeling for 0.5, 3.5, 6.5, 9.5, 12.5, 15.5, 18.5, 21.5, and 24.5 h in Emx1-*Upf2*cKO cortices (red) and the littermate control (black). The data are presented as the mean of two to six brains per time point, and for each brain, four 100-μm bins were quantified in each section, and three sections were quantified in total. The color-coded arrows indicated the time point at which the percentage of labeled RGCs reached a plateau ($T_C - T_S$). The value of R-squared was larger than 0.95 in both groups, and the formula was used to calculate the cell-cycle phases (T_C and T_S).

(I) Table of cell-cycle phases (T_C and T_S) calculated from (H) in E15.5 Emx1-*Upf2*cKO cortices and their littermate controls.

See also Figure S4.
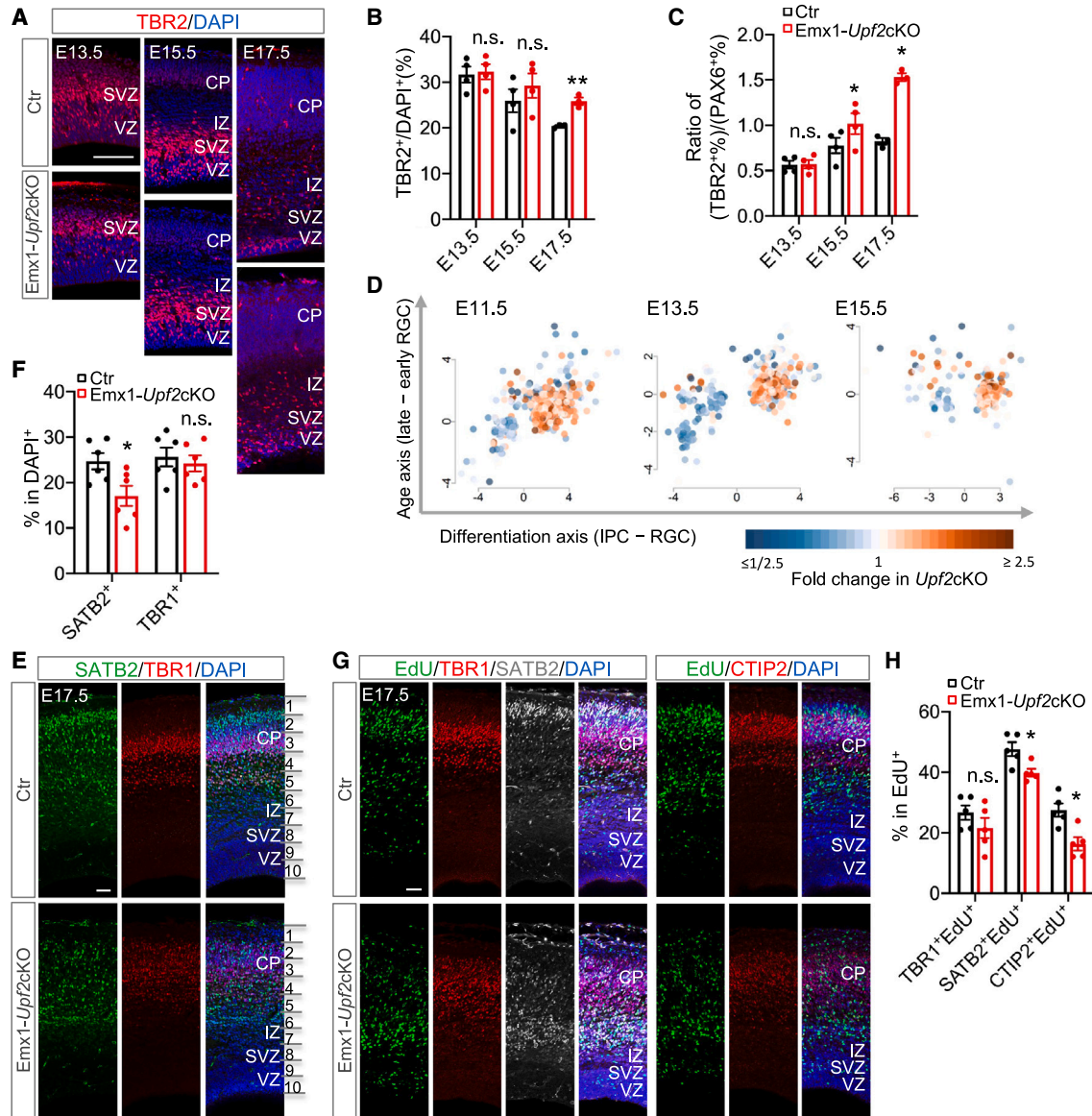
CellPress

Figure 4. Cell lineage defects in *Upf2*cKO mice

(A) Immunostaining of TBR2 in E13.5, E15.5, and E17.5 Emx1-*Upf2*cKO cortices and their littermate controls (scale bars, 100 μm).

(B and C) Quantification of the percentage of TBR2$^+$ cells in 100-μm bin and (TBR2$^+$%) / (PAX6$^+$%) in E13.5, E15.5, and E17.5 Emx1-*Upf2*cKO cortices and their littermate controls (n = 3–4; N = 3–4 images per section, 2–3 sections per sample).

(D) A scatter plot shows differentially expressed genes (DEGs) between IPC and RGC or between late RGC and early RGC. Differential expression values of DEGs (in either x or y axis) between two conditions (log$_2$(CPM$_1$ + 1) −log$_2$(CPM$_2$ + 1)) are plotted on the differentiation x axis (E13IPC−E11RGC, E15IPC−E13RGC, and E17IPC−E15RGC, respectively) vs. age y axis (E13RGC−E11RGC, E15RGC−E13RGC, and E17RGC−E15RGC, respectively). Gene expression values were downloaded from GSE107122. For each gene, their gene expression fold change in *Upf2*cKO (log$_2$(TPM$_{KO}$ + 1) −log$_2$(TPM$_{Ctr}$ + 1)) was color coded.

(E) Immunostaining of layer markers SATB2 and TBR1 in E17.5 Emx1-*Upf2*cKO cortices and their littermate controls (scale bars, 50 μm).

(F) Quantification of the percentages of SATB2$^+$ cells and TBR1$^+$ cells in 100-μm bin of E17.5 Emx1-*Upf2*cKO cortices and their littermate controls (n = 6; N = 2–3 images per section, 2–3 sections per sample).

(G and H) To estimate the production of layer VI neurons (TBR1$^+$EdU$^+$), layer II-V neurons (SATB2$^+$EdU$^+$), and layer V neurons (CTIP2$^+$EdU$^+$) in *Upf2*cKO cortices, pregnant mice were injected with EdU (100 mg/kg) at E14.5 and analyzed at E17.5. Representative confocal images were shown (G; scale bars, 50 μm), and quantification of EdU$^+$ cells with different layer markers was shown in (H) (n = 5; N = 2 images per section and 3 sections per group).

See also Figures S4–S6.

we derived DEGs between IPCs and RGCs, which represent the RGC-to-IPC transition (the differentiation axis), and between RGC clusters of different ages representing the early RGC-to-late RGC transition (the age axis). We plotted the differentiation signals of these genes by these two axes (Figure 4D). Some genes exhibit a larger fold change in the differentiation compared with the age axis, whereas others show a larger fold change in the age compared with the differentiation axis. We term all these genes collectively as RLT genes.

NMD's impact on RGC transcriptomes was mapped onto these two transitions: the RGC-to-IPC and the early RGC-to-late RGC. We tested whether the RLT genes are mis-regulated in Emx1-*Upf2*cKO and found that NMD-dependent genes are significantly more enriched in the differentiation axis (Figure 4D, each gene is color coded by its fold change in *Upf2*cKO). The enrichment of NMD-dependent genes on the differentiation axis was significant at E11.5, E13.5, and E15.5 (p value = 1.1×10^{-31}, 7.9×10^{-20}, and 2.0×10^{-19}, respectively), suggesting that this NMD dependency is continual and intrinsic to the RGC-to-IPC transition. Importantly, the upregulated genes in the *Upf2*cKO (brown dots in Figure 4D) tend to be IPC genes (i.e., upregulated in IPC vs. RGC). Therefore, the direction of these differentiation signals agrees with that NMD inhibits the RGC-to-IPC transition.

By contrast, fewer NMD-dependent genes were detected along the age axis, suggesting that NMD has a less regulatory action in the transition from early RGCs-to-late RGCs. The NMD regulatory direction did not correlate with the age direction. In summary, NMD regulation in RGC mainly restrains its transition to become IPC and exerts a nondirectional influence on the early-to-late RGC transition.

We also performed snRNA-seq from an E15.5 Emx1-*Upf2*cKO mouse cortex and control littermate (Figure S5D). We examined the cell-cycle phase distribution among RGCs and found that the M/G1 phase increased from 40.98% in WT to 66.81% in Emx1-*Upf2*cKO. The S-phase RGCs decreased from 22.93% in WT to 13.37% *Upf2*cKO (Figure S5E). Among the proliferating NPCs, *Pax6*-, *Top2a*-, or *Nes*-expressing RGCs were uniformly decreased in the *Upf2*cKO (Figure S5F). IPC marker-expressing cells show variable changes by distinct markers.

Reduced upper-layer neurons in Emx1-*Upf2*cKO mice

We examined whether neurogenesis was affected in Emx1-*Upf2*cKO mice. During development, cortical neural progenitors alter their cell competence and produce waves of distinct projection neurons that migrate radially toward the pial surface in an "inside-out" manner (Figure 1A). As a result, early-born neurons reside in the lower layers, whereas late-born neurons form the upper layers. Interestingly, we observed little difference in TBR1+ layer VI deeper layer neurons but a significant decrease in SATB2+ layer II–V neurons in E17.5 Emx1-*Upf2*cKO neocortices (Figures 4E, 4F, S6A, and S6B).

The reduction in SATB2+ neurons arose from a deficiency in neural progenitors. In Nex-*Upf2*cKO mice, where *Upf2* was knocked out right after mitosis, the number and lamination of SATB2+ and TBR1+ neurons were not affected (Figures S6C–S6E), indicating that the neuronal defects in Emx1-*Upf2*cKO cortices originate from the deficiency in neural progenitors.

Taking all the data, we reasoned that slower RGC division and increased RGC-to-IPC transition collectively reduce the RGC pool in Emx1-*Upf2*cKO mice over time. Because late RGCs (E15 and onward) are more reduced compared with early RGCs (before E15) in *Upf2*cKO (Figures 3A and 3B), upper-layer neurons are more affected in the mutant. The reduction of upper-layer neurons explains the microcephaly of Emx1-*Upf2*cKO mice.

An alternative hypothesis is that progenitor cells preferentially commit the lower-layer neuron fate rather than the upper-layer neuron fate. The delayed switch in competence amplified the reduction in the RGC pool to generate even fewer upper-layer neurons. To test this, we compared WT and Emx1-*Upf2*cKO for their neuronal outputs regarding the laminar fate. We labeled cycling progenitors with EdU (100 μg/g body weight i.p.) at E14.5 and measured the number and distribution of neuronal subtypes (TBR1, SATB2, and CTIP2) among EdU+ cells in the cortical plate 3 days afterward. In the Emx1-*Upf2*cKO cortex layer II–V SATB2+ neurons and layer V CTIP2+ were significantly reduced among EdU+ neurons (Figures 4G and 4H). Importantly, layer VI TBR1+ neurons did not increase at the cost of upper-layer neurons but decreased slightly, although statistically insignificantly. Therefore, *Upf2*KO progenitors do not delay the change in their competence from lower-layer neuron fate to upper-layer neuron fate. The absence of a substantial change in cell fate competence is consistent with prior transcriptomic analyses that NMD exerts an uncoordinated influence on the early-to-late RGC transition (Figure 4D).

CRISPRi screening identified genetic modifiers of *Upf2*KO NPC growth defect

To identify genetic modifiers rescuing the growth defects, we conducted CRISPRi screening in the *Upf2*fl/fl NPC model. Because *Upf2*KO mostly upregulates target genes, a cell fitness screen with CRISPRi knockdown would identify functional effectors whose induction by *Upf2*KO accounts for the cell proliferation defect. This CRISPRi screen would also reveal genetic suppressors that neutralize *Upf2*KO's effects. We thought screening regulators of gene expression would have a better success. We therefore generated a customized library of 3,600 sgRNAs targeting the transcription start sites (TSS) of 720 transcription factors, epigenetic factors, and RNA-binding protein genes (Figure S7A). The hits from primary NPC screens would be more relevant.

We first infected *Upf2*fl/fl NPCs with dCas9-Krab lentivirus to construct the dCas9-Krab-expressing stable NPC lines. Different NPC lines were compared for their CRISPRi efficiency with the Tag Red Fluorescent Protein 657 (TagRFP657) validation system (Figures S7B and S7C).[61] Two NPC lines with the highest efficiency were selected for the final screens. For the final screens, the sgRNA library was infected at <20% positive rate (Figures S7D and S7E).[61] Cells were then infected with Cre lentivirus to induce *Upf2*KO or with GFP lentivirus as a control. Because *Upf2*KO NPCs proliferated slower than residual uninfected cells in the Cre virus group, we added additional Cre virus from 48 to 72 h to assure high KO efficiency over time. Principal-component analysis (PCA) of sgRNA distributions showed that experimental groups separated well, and the two
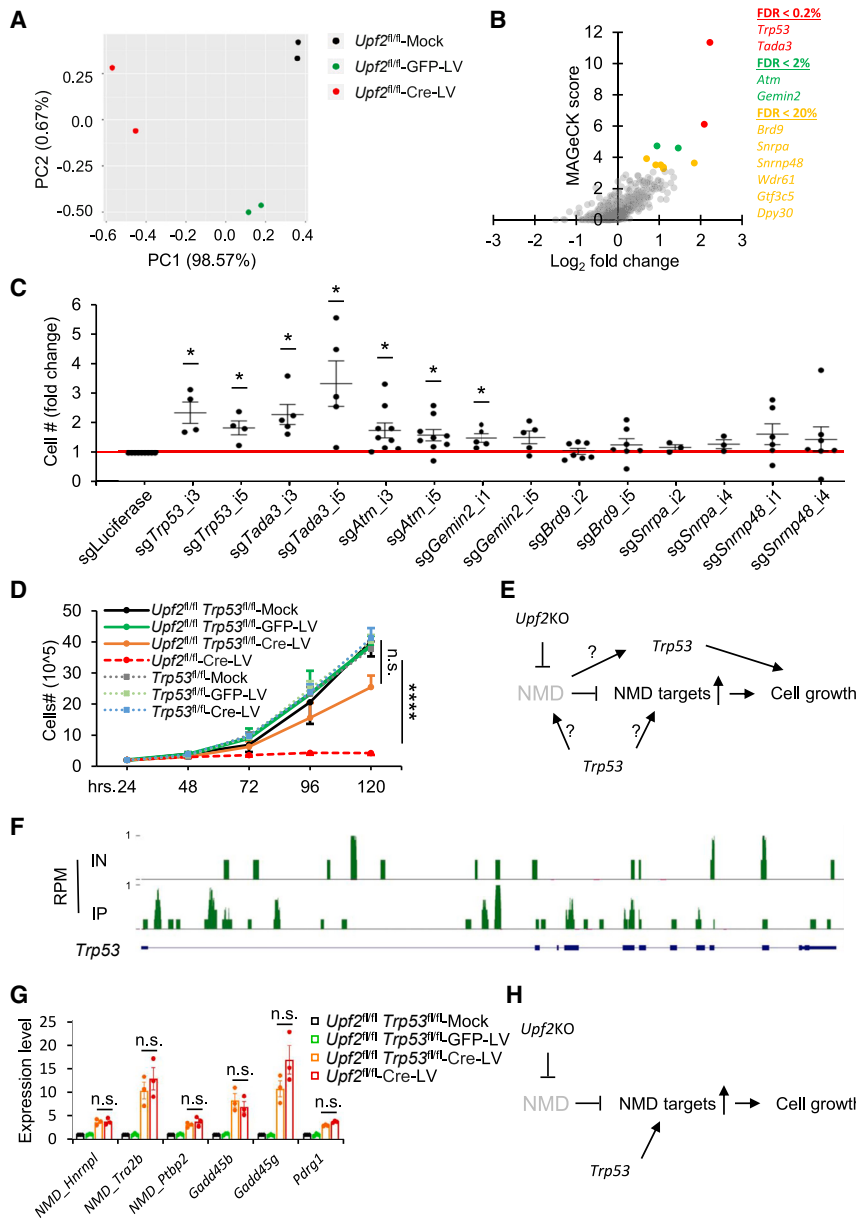
Figure 5. CRISPRi screening of *Upf2*KO NPCs

(A) PCA analysis showed reproducibility between two dCas9-KRAB-expressing *Upf2*fl/fl NPC cell lines and clear separation among experimental groups.

(B) MAGeCK score plot showed multiple hits identified in CRISPRi screening, including *Trp53*.

(C) Validation of CRISPRi screening hits in Cre-infected dCas9-KRAB-expressing *Upf2*fl/fl NPC cell lines (*n* = 3–9).

(D) *Upf2 Trp53*dKO showed a clear cell growth rescue compared with *Upf2*KO, whereas *Trp53*KO alone did not clearly affect cell proliferation (data are analyzed by the two-way ANOVA; *n* = 4).

(E) Possible mechanisms for *Trp53* depletion rescuing *Upf2*KO-induced cell growth defect.

(F) UPF1 eCLIP-seq showed no signal enrichment in *Trp53*, including the 3′UTR. Scale represents reads per million (RPM) mapped to the *Trp53*.

(G) *Upf2 Trp53*dKO had a similar expression profile of the NMD targets compared with *Upf2*KO (*n* = 3).

(H) *Trp53* and NMD co-regulated genes that inhibited cell growth in *Upf2*KO NPCs.

See also Figures S7 and S8 and Table S2.

pathway. We selected two sgRNAs per gene from our top seven hits for verification (Table S2). Compared with the sgLuciferase control, top hits *Trp53* and *Tada3* showed the most efficient rescue of the NPC growth (Figure 5C). Two sgRNAs of *Atm*, *Gemin2*, and *Snrnp48* showed moderate rescue effects. Among all, *Trp53* appeared as the most attractive hit for further investigation.

*Trp53*KO rescues *Upf2*KO-induced growth defect

Next, we bred *Trp53*fl/fl with *Upf2*fl/fl mouse line and used their F1s to produce *Trp53*fl/fl *Upf2*fl/fl mouse lines, from which we derived primary *Upf2*fl/fl *Trp53*fl/fl NPCs from E14 neocortices. We then infected *Upf2*fl/fl *Trp53*fl/fl NPC lines with Cre lentivirus to simultaneously knock out *Upf2* and *Trp53* and monitored their growth. Both *Upf2 Trp53*dKO NPCs and *Trp53*KO NPCs grew significantly more than the *Upf2*KO groups (Figure 5D). We performed EdU labeling in *Upf2 Trp53*dKO NPCs and found the percentage of EdU+ NPCs among all NPCs was similar between *Upf2 Trp53*dKO NPCs and control groups, suggesting that this rescue was due to the normalization of cell cycle progression (Figures S8A–S8D).

How does *Trp53*KO rescue *Upf2*KO-induced growth defect? One possibility is that *Trp53* is a downstream target of *Upf2* (Figure 5E). However, UPF1 enhanced cross-linking immunoprecipitation and high-throughput sequencing (eCLIP-seq) in NPCs (see below) did not detect *Trp53* mRNA as the NMD target (Figure 5F). We detected no change in TRP53 proteins in *Upf2*KO NPCs (Figures S8E–S8G). Furthermore, *Trp53* mRNA expression

NPC lines yielded similar results (Figure 5A). The major variance was explained by PC1 (98.57%), under which the Cre-LV groups (aka, *Upf2*KO) were well separated from the GFP-LV and Mock groups.

Comparing the Cre-LV and GFP-LV groups,[62] genes with an increased sgRNA frequency (log₂FC > 0.6) and a FDR < 20% in the Cre-LV group were considered potential hits. With FDR < 0.2%, *Trp53* and *Tada3* were identified as the top two hits. At FDR < 2%, *Atm* and *Gemin2* emerged as other two hits. With FDR < 20%, *Brd9*, *Snrpa*, *Snrnp48*, *Wdr61*, *Gtf3c5*, and *Dpy30* appeared as additional rescue genes (Figure 5B; Table S2). TADA3 was reported as a binding protein of human TP53 and could enhance the activity of the p53 pathway.[63] Ataxia telangiectasia mutated (ATM) kinase is also known to activate TP53.[64–66] These top three hits were linked to the p53

was not changed in *Upf2*cKO cortices *in vivo* (Figure S8H). Therefore, there is no evidence to support *Trp53* as a direct target of UPF2 responsible for the growth defect of *Upf2*KO NPCs.

Could TRP53 depletion bypass UPF2 deletion to restore NMD activity in NPCs (Figure 5E)? We checked the known NMD targets in *Upf2 Trp53*dKO NPCs and found that they remained as elevated as in *Upf2*KO NPCs (Figure 5G). Therefore, *Trp53*KO did not globally reverse the NMD inhibition to rescue *Upf2*KO. These data suggest that the *Trp53* activity intersects with NMD regulation in controlling the NPC cell cycle (Figure 5H). They also imply that most NMD targets have a marginal effect on the cell cycle.

The intersection between NMD regulation and TRP53 targets in NPCs

We examined the transcriptomic changes in neural progenitors using scRNA-seq and scored cells by 688 signature genes associated with each cell-cycle phase: M/G1, G1/S, S, G2, and G2/M.[67] Only six of the 688 signature genes for cell-cycle phase classification were differentially expressed in *Upf2*KO NPCs, supporting this approach to classify cell state. We delineated phase-dependent NMD regulation and found 105, 88, 86, 72, and 74 upregulated genes (details in STAR Methods) in M/G1, G1/S, S, G2, and G2/M, respectively, totaling 138 nonredundant genes (Figure 6A; Table S3). Most genes were commonly upregulated in all five cell-cycle phases. Interestingly, 28 genes were uniquely upregulated in the M/G1 phase, 5 in G1/S, 4 in G2, 2 in S, and 2 in G2/M. The commonly upregulated genes also exhibited a larger magnitude of expression changes in the M/G1 phase compared with other phases (Figure 6B), suggesting that gene expression in M/G1 is the most affected by NMD inhibition. In contrast to the 138 upregulated genes, only 9 were downregulated, and all were in the M/G1 phase (Figure 6B). This is consistent with *Upf2* and NMD mainly functioning to degrade RNA. These data support a model in which gene upregulation in the M/G1 phase affects *Upf2*KO cells' transition from the M/G1 phase to the S phase. More *Upf2*KO NPCs are stalled in the G0_G1 phase and fewer entered the S phase (Figures 2M–2P). Randomly selected upregulated genes were validated *in vivo* (Figures S9A–S9C).

Gene Ontology (GO) analysis of these 138 upregulated genes showed significant enrichment of the p53 transcriptional gene network (Figure 6C). Another significant GO term is "positive regulation of programmed cell death." Because *Trp53* and its targets were known to be implicated in apoptosis, this GO term reflected the overrepresentation of the *Trp53* signaling pathway. Note that cell death was not apparent in *Upf2*KO NPCs (Figures S3K–S3N).

To determine the direct target of the NMD pathway, we performed UPF1 eCLIP-seq in NPCs (Figures S9D and S9E). The UPF1 binding sites in primary NPCs were enriched in the 3′UTR and the *de novo* motif analysis found "CCC" enriched in peaks (Figures S9F and S9G), consistent with previously published UPF1 eCLIP-seq data in immortalized cell lines.[68–70] Overlapping 4,146 eCLIP hits (Figure 6D and Table S4) with the upregulated DEGs in *Upf2*KO progenitors identified 78 high-confidence NMD-targeted genes (Figures S10A–S10J). The top GO term of these genes was the p53 signaling pathway (Figure 6E).[71]

We checked whether the CRISPRi hits were direct NMD targets. The *Trp53* gene is not bound by UPF1 (Figure 5F). Except *Atm* passing the threshold ($-\log_{10}(p$ value) > 5) and *Gemin2* with a mild ($-\log_{10}(p$ value) = 2.59) enrichment, *Tada3*, *Brd9*, *Snrpa*, and *Snrnp48* did not show peaks of UPF1 eCLIP signals (Figures 5F and S11). Therefore, the CRISPRi hits are more likely genetic modifiers rather than direct effectors of NMD inhibition in regulating NPC division.

Because *Trp53*KO rescued cell growth defects of *Upf2*KO progenitors, we reasoned that functional effectors of *Upf2*KO could be identified by comparing the transcriptomes of WT, *Upf2*KO, and dKO NPCs using bulk mRNA-seq (Figure S12A). We compared gene expression levels in *Upf2*KO and WT samples: 355 were upregulated (fold change $\geq$ 2, FDR $\leq$ 0.05), and 78 were downregulated (fold change $\leq$ 0.5, FDR $\leq$ 0.05) (Figure S12B). Next, we determined which mis-regulated genes were reverted by comparing *Upf2 Trp53*dKO and *Upf2*KO (Figure S12C).

Among 355 upregulated genes, 298 (83.9%) showed insignificant changes between *Upf2*KO and *Upf2 Trp53*dKO, indicating that, at the molecular level, NMD inhibition was not globally rescued by *Trp53*KO. On the other hand, 55 *Upf2*KO-induced genes were significantly downregulated by *Trp53*KO (Figure 6F; Table S5). The top GO terms of these rescued genes pointed to the p53 regulation network and "negative regulation of cell population proliferation" (Figure 6G).[71] This supports our hypothesis that the intersecting regulation between the p53 pathway and the NMD pathway is suppressing cell proliferation and division. The downregulation of these genes in the *Upf2 Trp53*dKO is consistent with the rescue of *Upf2*KO NPCs by *Trp53*dKO.

Overlapping the eCLIP-Seq, *Upf2*KO/dKO bulk mRNA-seq, and scRNA-seq results gave five high-confidence effector candidates: *Cdkn1a*, *Ak1*, *Crip2*, *Phlda3*, and *Sesn2* (Figure 6H). The expression of *Cdkn1a*, *Ak1, Phlda3*, and *Sesn2 in vivo* exhibited 2.93-, 1.24-, 2.14-, and 5.44-fold increases in Emx1-*Upf2*cKO cortices, respectively (Figures S12D–S12G). All five genes showed a clear pattern of gene expression upregulation in *Upf2*KO, reversion in *Upf2 Trp53*dKO *in vitro* (Figures S13A–S13E), and significantly enriched UPF1 binding signals in their 3′UTRs (Figures 7D and S13F–S13I). We further confirmed these changes by detecting the increased protein levels of AK1 and SESN2 in *Upf2*KO NPCs and a decrease in *Upf2 Trp53*dKO NPCs (Figures S13J–S13L), consistent with RNA level changes (Figure S13E).

Cdkn1a is a direct NMD target diminished by *Trp53*KO to rescue growth defects of *Upf2*KO NPCs

Cdkn1a (*p21*) is one of the most well-defined cell-cycle checkpoint genes.[72] It negatively mediates G1-to-S and G2-to-M transitions.[73,74] To test whether *Cdkn1a* was a genuine NMD target, we first detected the expression levels of *Cdkn1a* in *Upf2*KO NPCs. We found a ~6.3-fold increase in *Upf2*KO NPCs (Figure 7A). To test whether this induction was caused by transcription regulation, we designed RT-qPCR primers to measure the pre-mRNA expression level of *Cdkn1a*. We observed a modest 1.75-fold increase, substantially less than the 6.3-fold change at the mRNA level (Figure 7B).
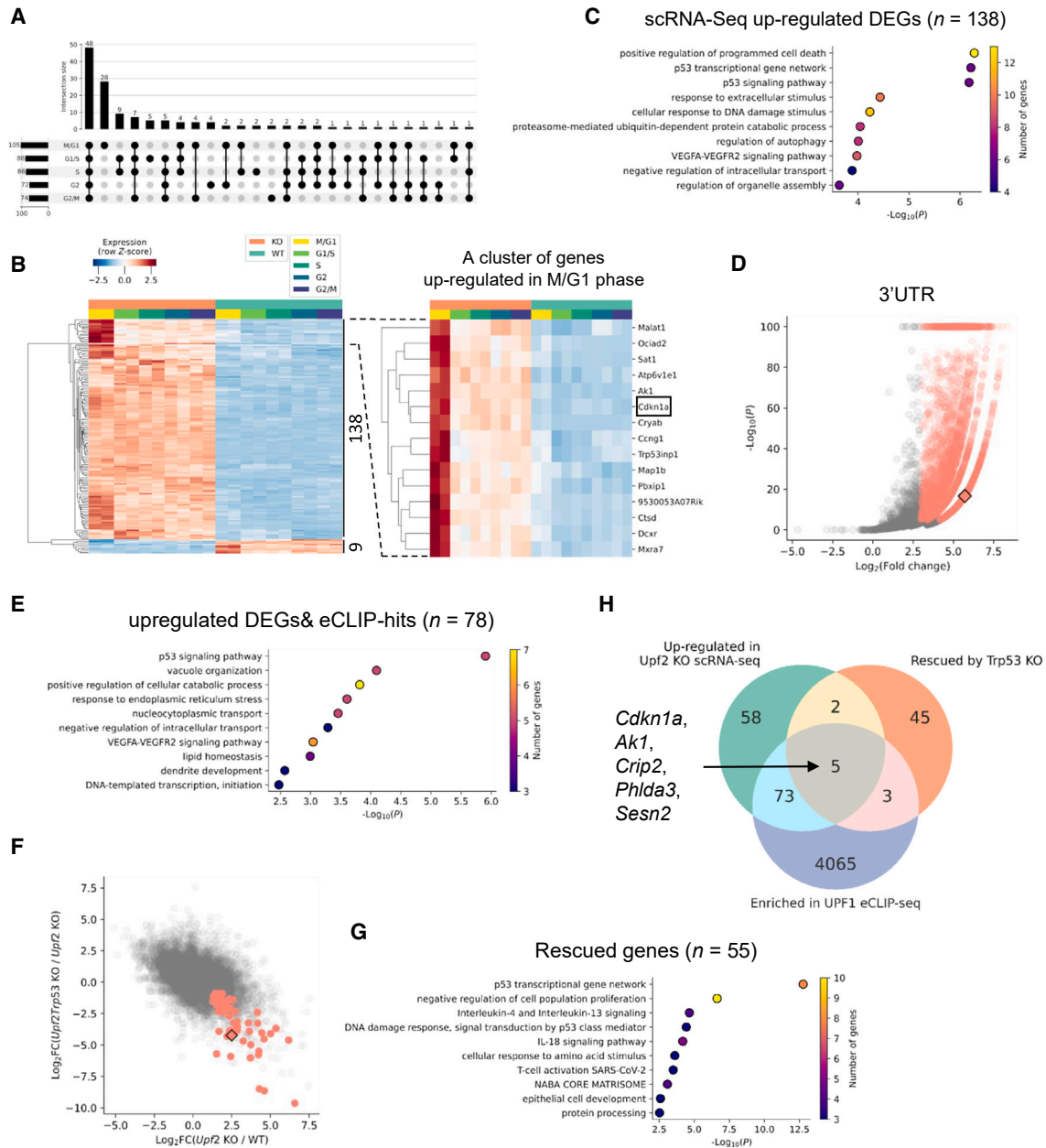
🤏 CellPress

Figure 6. Integrated functional genomics identified the intersection between the *Trp53* transcriptional pathway and *Upf2*KO-induced NMD targets

(A) Cell-cycle phase-dependent gene upregulation in *Upf2*KO NPCs.

(B) Heatmap showing the magnitude of differential gene expression comparing *Upf2*KO and WT NPCs. (*Cdkn1a* gene was highlighted by a rectangular box.)

(C) GO term enrichment analysis of 138 upregulated genes identified p53-related networks.

(D) UPF1 eCLIP-seq data in primary NPC showed fold change of IP/Input (x axis) vs. *p* value (y axis) of all detected genes. *Cdkn1a* gene was highlighted by a rectangular box. Note: genes with $-\log_{10}(p$ value$) \geq 100$ were clustered along the y = 100 line.

(E) Top enriched GO terms of overlapping genes from eCLIP-seq and scRNA-seq.

(F) Scatter plot showed gene expression fold changes of *Upf2*KO/WT on the x axis and of *Upf2 Trp53*dKO/*Upf2*KO on the y axis. Mis-regulated genes in *Upf2*KO NPCs reverted by *Trp53*KO were labeled in red with *Cdkn1a* gene highlighted by a rectangular box.

(G) 55 rescued genes by *Trp53*KO in *Upf2*KO NPCs were significantly enriched in the p53 regulatory network and inhibition of cell proliferation.

(H) Venn diagram analysis of the eCLIP-seq, *Upf2*KO/dKO bulk-seq, and scRNA-seq data gave five high-confidence candidates.

See also Figures S9–S13 and Tables S3, S4, and S5.
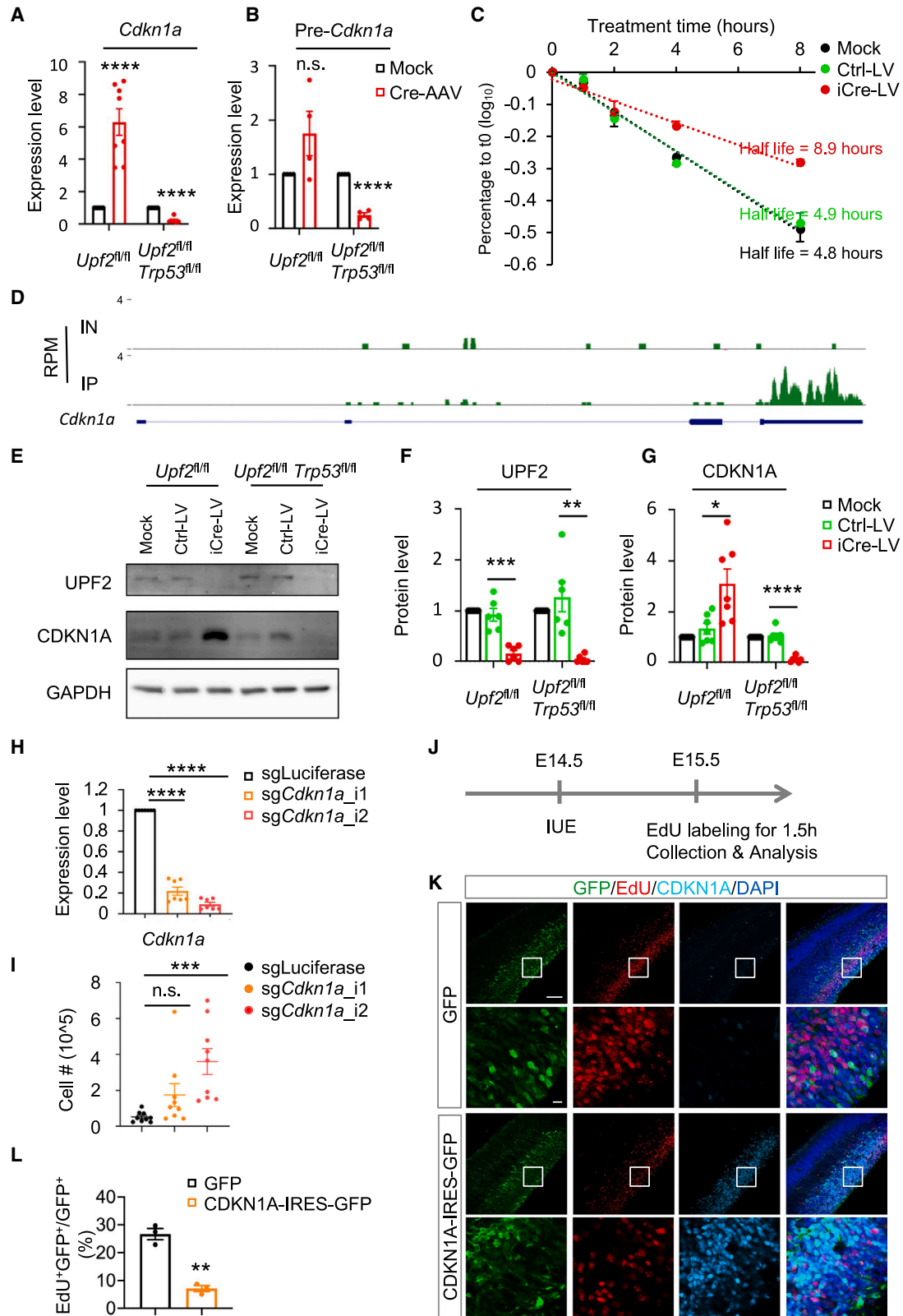
(legend on next page)

If *Cdkn1a* was targeted by NMD, its mRNA would become more stable in *Upf2*KO NPCs, leading to its upregulation. To test this, we performed the mRNA half-life test for Mock, Ctrl-LV-infected, and iCre-LV-infected NPCs with actinomycin D treatment. Compared with Mock (4.8 h) and Ctrl (4.9 h) groups, *Cdkn1a* mRNA had a clear longer half-life in iCre-LV-induced *Upf2*KO NPCs (8.9 h) (Figure 7C). Finally, UPF1 eCLIP data showed a clear signal in the 3′UTR of the *Cdkn1a* gene compared with the input (Figure 7D). We therefore concluded that *Cdkn1a* is a direct NMD target in primary NPC cells.

To validate the bulk RNA-seq findings, we also measured *Cdkn1a* mRNA in *Upf2 Trp53*dKO NPCs. Indeed, *Cdkn1a* was downregulated by ∼4.5-fold in dKO samples (Figure 7A). Importantly, in dKO samples, the pre-mRNA level was downregulated by ∼4.1-fold, consistent with the mRNA level change (Figure 7B). Therefore, the basally expressed *Trp53* in NPCs is necessary for *Cdkn1a* transcription, and *Trp53* deletion turns off *Cdkn1a* transcription, which abrogates the functional effect of *Upf2*KO on cell division.

To further examine the functional role of *Cdkn1a*, we tested the protein level of CDKN1A in *Upf2*KO and dKO NPCs. With the UPF2 protein removed (Figures 7E and 7F), *Upf2*KO NPCs exhibited a ∼3.6-fold upregulation of CDKN1A protein level, whereas dKO NPCs contained only ∼11% of CDKN1A proteins (Figures 7E and 7G). Because *Cdkn1a* is an essential cell cycle modulator and its upregulation slows or arrests cell cycle progression,[72,75] *Cdkn1a*, as the direct target of *Upf2*/NMD, is possibly the functional effector responsible for the growth defect of *Upf2*KO NPCs. To test this, two sgRNAs were chosen to specifically inhibit the expression of *Cdkn1a* (Table S2).[76] With RT-qPCR, we confirmed that both sgRNAs effectively inhibited the expression of *Cdkn1a* by 4.56-fold with the sgRNA_i1 and 10.9-fold with the sgRNA_i2 (Figure 7H). Functionally, compared with sgLuciferase control, *Cdkn1a* CRISPRi clearly increased cell growth of *Upf2*KO NPCs at 120 h after the Cre lentivirus infection (Figure 7I). Importantly, sgRNA_i2 showed a stronger effect than sgRNA_i1, indicating a dose-dependent effect.

With these established CRISPRi NPC lines, we also performed EdU labeling to test whether *Cdkn1a* knockdown rescued cell cycle progression in *Upf2*KO NPCs (Figures S14A–S14L). KD of *Cdkn1a* by sg*Cdkn1a*_i1 and i2 on top of Cre-mediated *Upf2*KO resulted in 26% to 30.3% of S-phase cells, significantly higher than those expressing sgLuciferase, demonstrating the

rescue effect of *Cdkn1a* depletion (Figures S14F and S14I). The rescue effects on S-phase cells were accompanied by a similar rescue effect on the G0_G1 phase (Figures S14J and S14K). Notably, the sg*Cdkn1a*_i2, with a higher CRISPRi efficiency of the two, showed a larger rescue effect.

CDKN1A regulates cell cycle progression in *Upf2*KO progenitors

To validate the functional role of *Cdkn1a* in NPC proliferation, we inserted *Cdkn1a*-ORF into a pCDH-CB lentiviral backbone to upregulate *Cdkn1a* expression. The EdU⁺ S-phase NPCs constitute a total population of 9.5% in the *Cdkn1a* overexpression group compared with 29.2% in the Ctrl group. The reduction in S-phase cells was accompanied by a significant increase in G0_G1 cells (Figures S15A–S15D).

We further test whether the overexpression of exogenous *Cdkn1a* can abolish the rescue effects of *Trp53*KO in *Upf2*KO progenitors. We first established *Upf2 Trp53*dKO NPCs by infecting *Upf2*^fl/fl *Trp53*^fl/fl NPCs with Cre lentivirus. The dKO NPCs can proliferate normally (Figure 5D). We then infected *Upf2 Trp53*dKO NPCs with Ctrl or *Cdkn1a*-expressing lentivirus. With the transduction of *Cdkn1a*-expressing lentivirus, the S-phase population was reduced and the G0_G1-phase population was increased. Therefore, *Cdkn1a* overexpression abolishes the cell-cycle rescue by *Trp53*KO (Figures S15E–S15H).

We tested whether CDKN1A upregulation could mimic the cell cycle defect of *Upf2*KO RGCs *in vivo*. We delivered the CDKN1A expression plasmid into E14.5 WT neocortices through *in utero* electroporation (IUE) and 1 day later performed EdU labeling for 1.5 h before collection (Figure 7J). The percentages of EdU⁺GFP⁺ in total GFP⁺-electroporated cells were measured in the control group (GFP) and CDKN1A overexpression group (CDKN1A-IRES-GFP). In Figures 7K and 7L, a significant decrease was found in CDKN1A-overexpressing GFP⁺ neural progenitors, indicating the defective proliferation, mimicking the effect of CDKN1A upregulation in *Upf2*KO progenitors *in vivo*.

We tested whether *Cdkn1a* loss of function in *Upf2*KO affected the cell cycle. We delivered the sh*Cdkn1a* plasmid via IUE into E14.5 embryonic cortices of litters generated by *Upf2*^fl/fl crossed with *Upf2*^fl/+;Emx1-Cre. We injected EdU at E16.5, after 1.5 h collected the brain, performed genotyping, and selected the *Upf2*^fl/fl;Emx1-Cre genotypes for further analyses (Figures S16A and S16B). In the contralateral cortex without plasmid electroporation, CDKN1A expression was

---

Figure 7. *Cdkn1a* is a direct NMD target whose upregulation is responsible for the *Upf2*KO NPC growth defect

(A) The expression level of *Cdkn1a* in Cre-AAV-infected *Upf2*KO and *Upf2 Trp53*dKO NPC samples (*n* = 8).

(B) The expression level of the *Cdkn1a* pre-mRNA in NPC samples (*n* = 4).

(C) Half-life test showed increased stability of *Cdkn1a* mRNA with *Upf2*KO (*n* = 4).

(D) UPF1 eCLIP-seq in primary NPCs showed UPF1 binding the 3′ UTR of *Cdkn1a*. Scale represents reads per million (RPM) mapped to *Cdkn1a* gene.

(E–G) Western blots showed CDKN1A protein level in *Upf2*KO and *Upf2 Trp53*dKO NPCs samples (*n* = 7). UPF2 and CDKN1A expressions were quantified in (F) and (G).

(H) RT-qPCR showed two sgRNAs inhibit the expression of *Cdkn1a* (*n* = 9).

(I) CRISPRi-mediated *Cdkn1a* knockdown partially rescued the growth defect in Cre-virus-infected *Upf2*KO NPCs. (*n* = 9).

(J) Strategy to deliver CDKN1A-IRES-GFP or control plasmids into cortical progenitors via *in utero* electroporation of WT embryos.

(K) GFP co-stained with CDKN1A and EdU (1.5 h labeling) in both CDKN1A-overexpressing group (CDKN1A-IRES-GFP) and control group (GFP) (scale bars, 100 μm in upper and 10 μm in lower images).

(L) Quantification of the percentage of proliferative EdU⁺GFP⁺ in total GFP⁺ in (K) (*n* = 3; 5 sections per group).
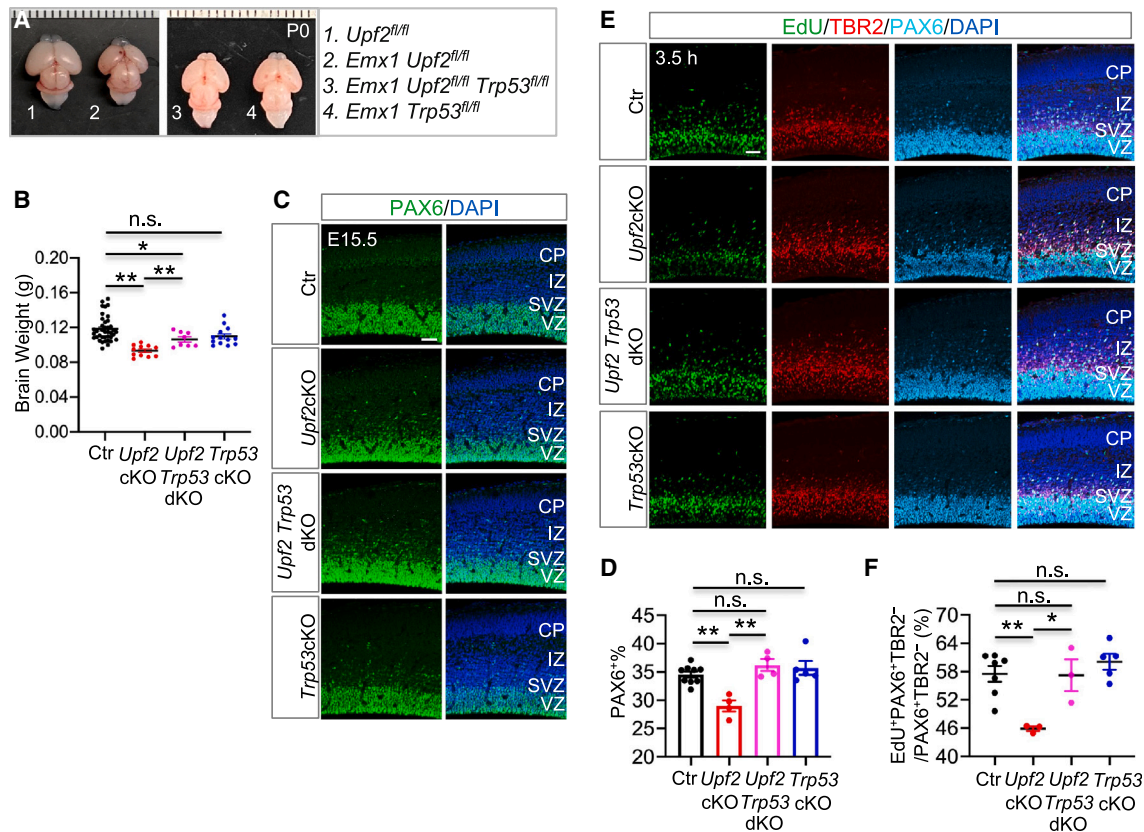
See also Figures S14–S16.

Figure 8. *Trp53*KO rescues microcephaly, RGC cell number, and cell cycle in Emx1-*Upf2*cKO mice *in vivo*

(A) Images of Emx1-*Upf2*cKO and Emx1-*Upf2 Trp53*dKO brains at P0.

(B) Brain weights of P0 Emx1-*Upf2*cKO, Exm1-*Upf2Trp53*dKO, and Emx1-*Trp53*cKO with their littermate control mice (n_C = 39; $n_{Upf2cKO}$=11; n_{dKO} = 8; $n_{Trp53cKO}$ = 13).

(C) Immunostaining of PAX6 in E15.5 *Upf2*cKO, *Upf2 Trp53*dKO, and *Trp53*cKO cortices (scale bars, 50 μm).

(D) Quantification of PAX6$^+$% cells in 100 μm bin of (C) (n_C = 9; $n_{Upf2cKO}$ = 4; n_{dKO} = 4; $n_{Trp53cKO}$ = 5; N = 2–3 images per section, 2–3 sections per sample).

(E) Representative immunofluorescent images of EdU with PAX6 and TBR2 in E15.5 *Upf2*cKO, *Upf2 Trp53*dKO, and *Trp53*cKO cortices after cumulative EdU labeling for 3.5 h (scale bars, 50 μm).

(F) Quantification of EdU$^+$PAX6$^+$TBR2$^-$% in total PAX6$^+$TBR2$^-$ RGCs in 100 μm bin of (E) (n_C = 7; $n_{Upf2cKO}$ = 3; n_{dKO} = 3; $n_{Trp53cKO}$ = 5; N = 4 images per section, 3 sections per sample).

See also Figure S17.

evident in the VZ (Figure S16B). In the ipsilateral cortex expressing sh*Cdkn1a*-IRES-EGFP, around 89.5% of GFP$^+$ cells became CDKN1A negative, confirming the efficiency of knockdown. To determine the proportion of *Upf2*KO progenitor cells labeled by EdU, we quantified the ratio of EdU$^+$ cells to DAPI$^+$cells in the VZ of the contralateral cortex as a baseline control. To determine the proportion of CDKN1A-depleted *Upf2*KO progenitor cells labeled by EdU, we quantified the ratio of EdU$^+$GFP$^+$ cells to total GFP$^+$ cells in the ipsilateral VZ. We found the CDKN1A-depleted GFP$^+$ cells exhibited a significant increase in the ratio (Figure S16C), showing the knockdown of CDKN1A partially rescued the proliferation defect in *Upf2*KO progenitors *in vivo*.

*Trp53*KO rescues progenitor cell defects and microcephaly of *Upf2*cKO mice *in vivo*

Given the *in vitro* rescue, we tested whether *Upf2*cKO phenotypes could be rescued by depletion of *Trp53 in vivo*. Strikingly,

we found that Emx1-*Upf2 Trp53*dKO mice did not exhibit microcephaly at birth (Figure 8A). The brain weight of dKO mice was significantly higher than Emx1-*Upf2*cKO and in the range of WT controls and *Trp53*cKO (Figure 8B). Emx1-*Upf2 Trp53*dKO contained PAX6$^+$ RGCs at a similar level to control littermates; meanwhile, *Trp53*cKO showed little effect on the number of PAX6$^+$ RGCs compared with the WT controls (Figures 8C, 8D, S17B, and S17C). These data are consistent with the notion that TRP53 depletion reverses the cell cycle defect of *Upf2*KO RGCs to prevent neonatal microcephaly. However, the TRP53 KO cannot rescue the survival rate of *Upf2*cKO mice (Figure S17A). Therefore, microcephaly is not the major cause of Emx1-*Upf2*cKO lethality. Microcephaly by itself is not necessarily lethal.

To verify the cell cycle impact of *Trp53*KO on *Upf2*KO RGCs *in vivo*, we performed cumulative EdU labeling in E15.5 *Upf2 Trp53*dKO mice (Figure 8E). The rescue was evident. For example, at the 3.5 h, EdU-labeled RGCs started to show a

CellPress

significant decrease in *Upf2*cKO, but not in dKO, compared with the controls (Figure 8F). About 57.5% of PAX6$^+$TBR2$^-$ RGCs were EdU-labeled in dKO, significantly higher than 45.9% in Emx1-*Upf2*cKO and comparable to 57.2% in the control or 60.1% in *Trp53*cKO (Figure 8F). We further estimated the T_C and T_S of RGCs in dKO to be 24.9 and 10.8 h, respectively, which were similar to the control littermates (Figures S17D and S17E). To further validate that TRP53 loss results in lowering CDKN1A level, we examined CDKN1A expression in E15.5 dKO brain sections (Figure S17F). With TRP53 deficiency, the upregulated CDKN1A signal in *Upf2*KO progenitors was completely reduced to a background level. CDKN1A expression in *Trp53*cKO and the control groups were both almost undetectable. Taken together, these data show *Trp53*KO rescues the cell-cycle defect of *Upf2*KO RGC and is sufficient to rescue the neonatal brain size reduction.

DISCUSSION

In this study, we showed that NMD, a regulated mRNA decay mechanism known for linking to multiple neurodevelopmental disorders, shapes the transcriptome and key cell cycle regulators to influence mammalian brain development *in vivo*. Another decay pathway mediated by m6A modification also prolongs the NSC cell cycle and brain development.[77] Inhibition of NMD in neural progenitors (*Upf2*cKO) leads to mouse microcephaly due to the prolonged cell cycle in RGCs. Mechanistically, NMD post-transcriptionally degrades a subset of TRP53's transcriptional targets to ensure sufficient progenitor cell divisions during brain development. Transcriptomic analysis also demonstrated the impact of NMD inhibition on RGC-to-IPC lineage transition, suggesting that NMD generally restrains IPC production.

Our studies reveal cell-type-specific phenotypes of NMD inhibition. Emx1-*Upf2*cKO reduces RGCs, increases IPCs, decreases upper-layer neurons, and does not significantly change lower-layer neurons. Although *Upf2*cKO promoted the RGC-to-IPC transition, it did not increase neuronal output. Therefore, in intact animals, NMD inhibition does not simply promote or inhibit differentiation as in culture studies. Altogether our study shows a novel mechanism of how NMD regulation selectively influences RGC maintenance and lineage progression to control neurogenesis.

Post-transcriptional NMD regulation overlaps with TRP53-dependent transcriptional regulation in finetuning cell division of NPCs

Human *TP53β* and *TP53γ*, two minor isoforms following splicing of exons 9β and 9γ, contained PTCs and were subjected to NMD regulation.[78,79] The major isoform *TP53α*, representing over 90% of total *TP53*, was not inhibited by NMD.[78] Human exons 9β and 9γ are not conserved or found in mouse *Trp53* (Figures S17G and S17H). We did not detect any cryptic exons within mouse intron 9 in *Upf2*KO RNA-seq samples either.

Human TP53 exerts some brakes on the cell cycle, and its removal can promote cell cycle progression, as genes for cell cycle regulation contain high-affinity binding sites for TP53.[80–82] TP53 regulates the transcriptional level of *CDKN1A* by binding to two TP53-responsive sites in the *CDKN1A* pro-

moter region.[83] *CDKN1A* mRNA has one of the shortest half-lives among TP53 target genes, indicating post-transcriptional control.[84] Our research shows that the nonsense-mediated RNA decay pathway functions as a crucial yet overlooked mechanism of *Cdkn1a* regulation.

Overall, cell cycle lengthening and a longer S phase in *Upf2*KO RGCs (Figures 3G–3I) agree with previous reports that the induction of *Cdkn1a* is critical for G1 arrest in cell lines.[85,86] Importantly, gene expression in *Upf2*KO NPCs is most affected in M/G1, and *Cdkn1a* is one of the most upregulated genes in the M/G1 phase (Figures 6A and 6B). As one of the strongest cell-cycle modulators, CDKN1A indirectly controls over 250 cell cycle-related genes.[87] Many DEGs in *Upf2*KO may be downstream of CDKN1A upregulation.

By selectively degrading *Cdkn1a* and other TRP53 transcriptional targets, NMD attenuates TRP53's influence on the NPC cell cycle, assuring the correct number of RGC cell divisions for brain development. Basal TRP53 activity is probably required in progenitors to maintain genome stability and to induce cell death upon severe damage. A collateral consequence is the expression of CDKN1A and other cell cycle checkpoint genes, which, at certain levels, limit cell cycle progression. The emergence of NMD-regulating *Cdkn1a* during evolution may have therefore contributed to the continual expansion of the progenitor cell pool and the increase in brain size in mammals.

Upf2cKO mice show distinct phenotypes compared with EJC mutants

The core exon junction complex (EJC) is deposited 20–24 nt upstream of the exon-exon junction and interacts with UPF2, providing a mechanistic link to explain the EJC branch of the NMD pathway.[88,89] That is, an mRNA transcript with a PTC >50 nt upstream of an exon-exon junction is generally targeted by NMD (aka the 50-nt rule). The heterozygote mutant mice of three core EJC components (*Magoh*, *Rbm8a*, and *Eif4a3*) exhibit defective neurogenesis and microcephaly.[90–94] Because EJC factors play a role in degrading PTC transcripts following the 50-nt rule, NMD inhibition could have underlined the EJC mutant phenotypes, or maybe not.

We initially suspected that *Upf2*cKO microcephaly could have shared a similar cellular phenotype with EJC mutants. Our subsequent analyses revealed distinct differences between *Upf2*cKO and EJC heterozygotes. For example, Magoh$^{+/-}$ prolongs mitosis without altering the S-phase length, and because the M phase consists of a short duration within a cell cycle,[94] the overall cell cycle length in Magoh$^{+/-}$ is not much affected. In contrast, *Upf2*cKO lengthens the overall cell cycle significantly and affects the S phase. Second, mitotically delayed Magoh$^{+/-}$ progenitors tend to produce more neurons,[94] but *Upf2*cKO progenitors do not (Figures 4G and 4H). Third, none of the *Magoh*, *Rbm8a*, or *Eif4a3* mutants increased TBR2$^+$ IPCs.[92] *Magoh* heterozygote brains actually showed a significant reduction in the number of IPCs.[90] However, *Upf2*KO promotes the RGC-to-IPC transition, and more TBR2$^+$ IPCs are detected in the progenitor pool.

Furthermore, haploinsufficiency for core EJC complex components generally caused more severe microcephaly phenotypes compared with the *Upf2*cKO. The *Magoh* heterozygotes

exhibited microcephaly around E12.5. Under the Emx1-Cre background, *Eif4a3*^{fl/+} and *Rbm8a*^{fl/+} mice (i.e., conditional heterozygotes) showed microcephaly and loss of PAX6^{+} cells also as early as E12.5,[91,92] but *Upf2*^{fl/fl} (i.e., conditional homozygotes) brain size appears largely normal by E15.5. In the Emx1-*Upf2*cKO cortex, the microcephaly only progressively occurs around E17. The current biochemical model states that EJC works through UPF2 to affect NMD transcripts. If the phenotypes of EJC mutants were largely due to NMD defect, *Upf2*cKO should have elicited severe phenotypes. Finally, *Trp53* deletion in *Upf2*KO did not correct NMD targets with a downstream EJC (Figure 5G). That means RGC can proliferate nearly normally even with inhibition of the EJC branch of NMD targets. Therefore, the EJC mutant phenotype is likely driven by a more dominant mechanism compared with NMD.

STAR★METHODS

Detailed methods are provided in the online version of this paper and include the following:

- KEY RESOURCES TABLE
- RESOURCE AVAILABILITY
  - Lead contact
  - Materials availability
  - Data and code availability
- EXPERIMENTAL MODEL AND STUDY PARTICIPANT DETAILS
  - Animals
  - Generation of Mouse cortical neural progenitor cells
  - E. coli competent cells
- METHOD DETAILS
  - CellTiter-Glo Luminescent Cell Viability Assay
  - Mouse Brain Sectioning and Immunofluorescence Staining
  - Mouse NPCs lentivirus infection and growth curve test
  - RNA purification and quantitative RT-PCR analysis
  - EdU and BrdU Labeling
  - EdU Staining and Confocal Imaging
  - Analysis of Cell-cycle Parameters
  - *In Utero* Electroporation
  - RNA Sequencing Libraries Construction
  - RNA-Seq Analysis
  - Isolation of single nuclei from embryonic cortices for snRNA-Seq
  - Single cell/single nuclei RNA Sequencing Libraries Construction
  - Single-cell RNA-Seq Analysis
  - Apoptotic analysis for *Upf2*KO NPCs by flow cytometry
  - Analysis of cell cycle progression by EdU pulse labeling
  - Enhanced UPF1 CLIP analysis
  - Protein extraction and immunoblotting
  - Half-life measurement of *Cdkn1a* mRNA in mouse NPCs
  - Lentivirus production with HEK 293T cells
  - Construction of *Upf2*^{fl/fl}-NPC-dCas9-Krab cells
  - Epigenetic CRISPR interference (CRISPRi) library screen
  - Epigenetic CRISPR interference (CRISPRi) positive hits verification
- QUANTIFICATION AND STATISTICAL ANALYSIS

SUPPLEMENTAL INFORMATION

Supplemental information can be found online at https://doi.org/10.1016/j.neuron.2024.04.006.

ACKNOWLEDGMENTS

AUTHOR CONTRIBUTIONS

Conceptualization, S.Z.; methodology, L.L., J.Z., L.C., and S.Z.; formal analysis, L.L., J.Z., N.K., Y.-L.L., L.P.N., L.Y., B.A.Y., L.C., and S.Z.; investigation, L.L., J.Z., Z.L., Y.-L.L., L.P.N., S.P.P., R.C., and S.M.B.; writing—original draft, L.L., J.Z., and S.Z.; writing—review & editing, L.L., J.Z., and S.Z.; visualization, L.L., J.Z., N.K., L.Y., S.M.B., B.A.Y., L.C., and S.Z.; supervision, G.W.Y., C.-W.C., L.C., and S.Z.; project administration, S.Z.; funding acquisition, L.C. and S.Z.

DECLARATION OF INTERESTS

The authors declare no competing interests.

REFERENCES

1. Lykke-Andersen, S., and Jensen, T.H. (2015). Nonsense-mediated mRNA decay: an intricate machinery that shapes transcriptomes. Nat. Rev. Mol. Cell Biol. *16*, 665–677. https://doi.org/10.1038/nrm4063.

2. He, F., and Jacobson, A. (2015). Nonsense-Mediated mRNA Decay: Degradation of Defective Transcripts Is Only Part of the Story. Annu. Rev. Genet. *49*, 339–366. https://doi.org/10.1146/annurev-genet-112414-054639.

3. Kashima, I., Yamashita, A., Izumi, N., Kataoka, N., Morishita, R., Hoshino, S., Ohno, M., Dreyfuss, G., and Ohno, S. (2006). Binding of a novel SMG-1-Upf1-eRF1-eRF3 complex (SURF) to the exon junction complex triggers Upf1 phosphorylation and nonsense-mediated mRNA decay. Genes Dev. *20*, 355–367. https://doi.org/10.1101/gad.1389006.

4. Grimson, A., O'Connor, S., Newman, C.L., and Anderson, P. (2004). SMG-1 is a phosphatidylinositol kinase-related protein kinase required for nonsense-mediated mRNA Decay in Caenorhabditis elegans. Mol. Cell. Biol. *24*, 7483–7490. https://doi.org/10.1128/MCB.24.17.7483-7490.2004.

5. Chakrabarti, S., Bonneau, F., Schüssler, S., Eppinger, E., and Conti, E. (2014). Phospho-dependent and phospho-independent interactions of the helicase UPF1 with the NMD factors SMG5-SMG7 and SMG6. Nucleic Acids Res. *42*, 9447–9460. https://doi.org/10.1093/nar/gku578.

6. Lykke-Andersen, J., Shu, M.D., and Steitz, J.A. (2000). Human Upf proteins target an mRNA for nonsense-mediated decay when bound downstream of a termination codon. Cell *103*, 1121–1131. https://doi.org/10.1016/s0092-8674(00)00214-2.

7. Singh, G., Rebbapragada, I., and Lykke-Andersen, J. (2008). A competition between stimulators and antagonists of Upf complex recruitment governs human nonsense-mediated mRNA decay. PLoS Biol. *6*, e111. https://doi.org/10.1371/journal.pbio.0060111.

8. Rebbapragada, I., and Lykke-Andersen, J. (2009). Execution of nonsense-mediated mRNA decay: what defines a substrate? Curr. Opin. Cell Biol. *21*, 394–402. https://doi.org/10.1016/j.ceb.2009.02.007.

9. Popp, M.W.-L., and Maquat, L.E. (2013). Organizing principles of mammalian nonsense-mediated mRNA decay. Annu. Rev. Genet. *47*, 139–165. https://doi.org/10.1146/annurev-genet-111212-133424.

10. Chang, Y.-F., Imam, J.S., and Wilkinson, M.F. (2007). The nonsense-mediated decay RNA surveillance pathway. Annu. Rev. Biochem. *76*, 51–74. https://doi.org/10.1146/annurev.biochem.76.050106.093909.

11. Nguyen, L.S., Kim, H.-G., Rosenfeld, J.A., Shen, Y., Gusella, J.F., Lacassie, Y., Layman, L.C., Shaffer, L.G., and Gécz, J. (2013). Contribution of copy number variants involving nonsense-mediated mRNA decay pathway genes to neuro-developmental disorders. Hum. Mol. Genet. *22*, 1816–1825. https://doi.org/10.1093/hmg/ddt035.

12. Tarpey, P.S., Raymond, F.L., Nguyen, L.S., Rodriguez, J., Hackett, A., Vandeleur, L., Smith, R., Shoubridge, C., Edkins, S., Stevens, C., et al. (2007). Mutations in UPF3B, a member of the nonsense-mediated mRNA decay complex, cause syndromic and nonsyndromic mental retardation. Nat. Genet. *39*, 1127–1133. https://doi.org/10.1038/ng2100.

13. Addington, A.M., Gauthier, J., Piton, A., Hamdan, F.F., Raymond, A., Gogtay, N., Miller, R., Tossell, J., Bakalar, J., Inoff-Germain, G., et al. (2011). A novel frameshift mutation in UPF3B identified in brothers affected with childhood onset schizophrenia and autism spectrum disorders. Mol. Psychiatry *16*, 238–239. https://doi.org/10.1038/mp.2010.59.

14. Laumonnier, F., Shoubridge, C., Antar, C., Nguyen, L.S., Van Esch, H., Kleefstra, T., Briault, S., Fryns, J.P., Hamel, B., Chelly, J., et al. (2010). Mutations of the UPF3B gene, which encodes a protein widely expressed in neurons, are associated with nonspecific mental retardation with or without autism. Mol. Psychiatry *15*, 767–776. https://doi.org/10.1038/mp.2009.14.

15. Jolly, L.A., Homan, C.C., Jacob, R., Barry, S., and Gecz, J. (2013). The UPF3B gene, implicated in intellectual disability, autism, ADHD and childhood onset schizophrenia regulates neural progenitor cell behaviour and neuronal outgrowth. Hum. Mol. Genet. *22*, 4673–4687. https://doi.org/10.1093/hmg/ddt315.

16. Lou, C.H., Shao, A., Shum, E.Y., Espinoza, J.L., Huang, L., Karam, R., and Wilkinson, M.F. (2014). Posttranscriptional control of the stem cell and neurogenic programs by the nonsense-mediated RNA decay pathway. Cell Rep. *6*, 748–764. https://doi.org/10.1016/j.celrep.2014.01.028.

17. Alrahbeni, T., Sartor, F., Anderson, J., Miedzybrodzka, Z., McCaig, C., and Müller, B. (2015). Full UPF3B function is critical for neuronal differentiation of neural stem cells. Mol. Brain *8*, 33. https://doi.org/10.1186/s13041-015-0122-1.

18. Huang, L., Shum, E.Y., Jones, S.H., Lou, C.-H., Chousal, J., Kim, H., Roberts, A.J., Jolly, L.A., Espinoza, J.L., Skarbrevik, D.M., et al. (2018). A Upf3b-mutant mouse model with behavioral and neurogenesis defects. Mol. Psychiatry *23*, 1773–1786. https://doi.org/10.1038/mp.2017.173.

19. Florio, M., and Huttner, W.B. (2014). Neural progenitors, neurogenesis and the evolution of the neocortex. Development *141*, 2182–2194. https://doi.org/10.1242/dev.090571.

20. Lin, Y., Yang, J., Shen, Z., Ma, J., Simons, B.D., and Shi, S.-H. (2021). Behavior and lineage progression of neural progenitors in the mammalian cortex. Curr. Opin. Neurobiol. *66*, 144–157. https://doi.org/10.1016/j.conb.2020.10.017.

21. Noctor, S.C., Flint, A.C., Weissman, T.A., Dammerman, R.S., and Kriegstein, A.R. (2001). Neurons derived from radial glial cells establish radial units in neocortex. Nature *409*, 714–720. https://doi.org/10.1038/35055553.

22. Noctor, S.C., Martínez-Cerdeño, V., Ivic, L., and Kriegstein, A.R. (2004). Cortical neurons arise in symmetric and asymmetric division zones and migrate through specific phases. Nat. Neurosci. *7*, 136–144. https://doi.org/10.1038/nn1172.

23. Kalebic, N., and Huttner, W.B. (2020). Basal Progenitor Morphology and Neocortex Evolution. Trends Neurosci. *43*, 843–853. https://doi.org/10.1016/j.tins.2020.07.009.

24. Hevner, R.F. (2019). Intermediate progenitors and Tbr2 in cortical development. J. Anat. *235*, 616–625. https://doi.org/10.1111/joa.12939.

25. Götz, M., Stoykova, A., and Gruss, P. (1998). Pax6 controls radial glia differentiation in the cerebral cortex. Neuron *21*, 1031–1044. https://doi.org/10.1016/s0896-6273(00)80621-2.

26. Englund, C., Fink, A., Lau, C., Pham, D., Daza, R.A.M., Bulfone, A., Kowalczyk, T., and Hevner, R.F. (2005). Pax6, Tbr2, and Tbr1 are expressed sequentially by radial glia, intermediate progenitor cells, and postmitotic neurons in developing neocortex. J. Neurosci. *25*, 247–251. https://doi.org/10.1523/JNEUROSCI.2899-04.2005.

27. Pollen, A.A., Nowakowski, T.J., Chen, J., Retallack, H., Sandoval-Espinosa, C., Nicholas, C.R., Shuga, J., Liu, S.J., Oldham, M.C., Diaz, A., et al. (2015). Molecular identity of human outer radial glia during cortical development. Cell *163*, 55–67. https://doi.org/10.1016/j.cell.2015.09.004.

28. Nowakowski, T.J., Bhaduri, A., Pollen, A.A., Alvarado, B., Mostajo-Radji, M.A., Di Lullo, E., Haeussler, M., Sandoval-Espinosa, C., Liu, S.J., Velmeshev, D., et al. (2017). Spatiotemporal gene expression trajectories reveal developmental hierarchies of the human cortex. Science *358*, 1318–1323. https://doi.org/10.1126/science.aap8809.

29. Yuzwa, S.A., Borrett, M.J., Innes, B.T., Voronova, A., Ketela, T., Kaplan, D.R., Bader, G.D., and Miller, F.D. (2017). Developmental Emergence of Adult Neural Stem Cells as Revealed by Single-Cell Transcriptional Profiling. Cell Rep. *21*, 3970–3986. https://doi.org/10.1016/j.celrep.2017.12.017.

30. Hochgerner, H., Zeisel, A., Lönnerberg, P., and Linnarsson, S. (2018). Conserved properties of dentate gyrus neurogenesis across postnatal development revealed by single-cell RNA sequencing. Nat. Neurosci. *21*, 290–299. https://doi.org/10.1038/s41593-017-0056-2.

31. Cao, J., Spielmann, M., Qiu, X., Huang, X., Ibrahim, D.M., Hill, A.J., Zhang, F., Mundlos, S., Christiansen, L., Steemers, F.J., et al. (2019). The single-cell transcriptional landscape of mammalian organogenesis. Nature *566*, 496–502. https://doi.org/10.1038/s41586-019-0969-x.

32. Huang, W., Bhaduri, A., Velmeshev, D., Wang, S., Wang, L., Rottkamp, C.A., Alvarez-Buylla, A., Rowitch, D.H., and Kriegstein, A.R. (2020). Origins and Proliferative States of Human Oligodendrocyte Precursor Cells. Cell *182*, 594–608.e11. https://doi.org/10.1016/j.cell.2020.06.027.

33. Bhaduri, A., Sandoval-Espinosa, C., Otero-Garcia, M., Oh, I., Yin, R., Eze, U.C., Nowakowski, T.J., and Kriegstein, A.R. (2021). An atlas of cortical arealization identifies dynamic molecular signatures. Nature *598*, 200–204. https://doi.org/10.1038/s41586-021-03910-8.

34. Velmeshev, D., Perez, Y., Yan, Z., Valencia, J.E., Castaneda-Castellanos, D.R., Wang, L., Schirmer, L., Mayer, S., Wick, B., Wang, S., et al. (2023). Single-cell analysis of prenatal and postnatal human cortical development. Science *382*, eadf0834. https://doi.org/10.1126/science.adf0834.

35. Albert, M., Kalebic, N., Florio, M., Lakshmanaperumal, N., Haffner, C., Brandl, H., Henry, I., and Huttner, W.B. (2017). Epigenome profiling and editing of neocortical progenitor cells during development. EMBO J. *36*, 2642–2658. https://doi.org/10.15252/embj.201796764.

36. Homem, C.C.F., Repic, M., and Knoblich, J.A. (2015). Proliferation control in neural stem and progenitor cells. Nat. Rev. Neurosci. *16*, 647–659. https://doi.org/10.1038/nrn4021.

37. Gao, P., Postiglione, M.P., Krieger, T.G., Hernandez, L., Wang, C., Han, Z., Streicher, C., Papusheva, E., Insolera, R., Chugh, K., et al. (2014). Deterministic progenitor behavior and unitary production of neurons in the neocortex. Cell *159*, 775–788. https://doi.org/10.1016/j.cell.2014.10.027.

38. Takahashi, T., Nowakowski, R.S., and Caviness, V.S., Jr. (1996). The leaving or Q fraction of the murine cerebral proliferative epithelium: a general model of neocortical neuronogenesis. J. Neurosci. *16*, 6183–6196. https://doi.org/10.1523/JNEUROSCI.16-19-06183.1996.

39. Shum, E.Y., Jones, S.H., Shao, A., Chousal, J.N., Krause, M.D., Chan, W.-K., Lou, C.-H., Espinoza, J.L., Song, H.-W., Phan, M.H., et al. (2016). The Antagonistic Gene Paralogs Upf3a and Upf3b Govern Nonsense-Mediated RNA Decay. Cell *165*, 382–395. https://doi.org/10.1016/j.cell.2016.02.046.

40. Medghalchi, S.M., Frischmeyer, P.A., Mendell, J.T., Kelly, A.G., Lawler, A.M., and Dietz, H.C. (2001). Rent1, a trans-effector of nonsense-mediated mRNA decay, is essential for mammalian embryonic viability. Hum. Mol. Genet. *10*, 99–105. https://doi.org/10.1093/hmg/10.2.99.

41. Li, T., Shi, Y., Wang, P., Guachalla, L.M., Sun, B., Joerss, T., Chen, Y.-S., Groth, M., Krueger, A., Platzer, M., et al. (2015). Smg6/Est1 licenses embryonic stem cell differentiation via nonsense-mediated mRNA decay. EMBO J. *34*, 1630–1647. https://doi.org/10.15252/embj.201489947.

42. Weischenfeldt, J., Damgaard, I., Bryder, D., Theilgaard-Mönch, K., Thoren, L.A., Nielsen, F.C., Jacobsen, S.E.W., Nerlov, C., and Porse, B.T. (2008). NMD is essential for hematopoietic stem and progenitor cells and for eliminating by-products of programmed DNA rearrangements. Genes Dev. *22*, 1381–1396. https://doi.org/10.1101/gad.468808.

43. Gorski, J.A., Talley, T., Qiu, M., Puelles, L., Rubenstein, J.L.R., and Jones, K.R. (2002). Cortical excitatory neurons and glia, but not GABAergic neurons, are produced in the Emx1-expressing lineage. J. Neurosci. *22*, 6309–6314. https://doi.org/10.1523/JNEUROSCI.22-15-06309.2002.

44. Guo, H., Hong, S., Jin, X.L., Chen, R.S., Avasthi, P.P., Tu, Y.T., Ivanco, T.L., and Li, Y. (2000). Specificity and efficiency of Cre-mediated recombination in Emx1-Cre knock-in mice. Biochem. Biophys. Res. Commun. *273*, 661–665. https://doi.org/10.1006/bbrc.2000.2870.

45. Goebbels, S., Bormuth, I., Bode, U., Hermanson, O., Schwab, M.H., and Nave, K.-A. (2006). Genetic targeting of principal neurons in neocortex and hippocampus of NEX-Cre mice. Genesis *44*, 611–621. https://doi.org/10.1002/dvg.20256.

46. Tronche, F., Kellendonk, C., Kretz, O., Gass, P., Anlag, K., Orban, P.C., Bock, R., Klein, R., and Schütz, G. (1999). Disruption of the glucocorticoid receptor gene in the nervous system results in reduced anxiety. Nat. Genet. *23*, 99–103. https://doi.org/10.1038/12703.

47. Li, Z., Vuong, J.K., Zhang, M., Stork, C., and Zheng, S. (2017). Inhibition of nonsense-mediated RNA decay by ER stress. RNA *23*, 378–394. https://doi.org/10.1261/rna.058040.116.

48. Zhao, J., Li, Z., Puri, R., Liu, K., Nunez, I., Chen, L., and Zheng, S. (2022). Molecular profiling of individual FDA-approved clinical drugs identifies modulators of nonsense-mediated mRNA decay. Mol. Ther. Nucleic Acids *27*, 304–318. https://doi.org/10.1016/j.omtn.2021.12.003.

49. Kurosaki, T., Popp, M.W., and Maquat, L.E. (2019). Quality and quantity control of gene expression by nonsense-mediated mRNA decay. Nat. Rev. Mol. Cell Biol. *20*, 406–420. https://doi.org/10.1038/s41580-019-0126-2.

50. Nelson, J.O., Moore, K.A., Chapin, A., Hollien, J., and Metzstein, M.M. (2016). Degradation of Gadd45 mRNA by nonsense-mediated decay is essential for viability. eLife *5*, e12876. https://doi.org/10.7554/eLife.12876.

51. Karam, R., Lou, C.-H., Kroeger, H., Huang, L., Lin, J.H., and Wilkinson, M.F. (2015). The unfolded protein response is shaped by the NMD pathway. EMBO Rep. *16*, 599–609. https://doi.org/10.15252/embr.201439696.

52. Popp, M.W., and Maquat, L.E. (2015). Attenuation of nonsense-mediated mRNA decay facilitates the response to chemotherapeutics. Nat. Commun. *6*, 6632. https://doi.org/10.1038/ncomms7632.

53. Nowakowski, R.S., Lewin, S.B., and Miller, M.W. (1989). Bromodeoxyuridine immunohistochemical determination of the lengths of the cell cycle and the DNA-synthetic phase for an anatomically defined population. J. Neurocytol. *18*, 311–318. https://doi.org/10.1007/BF01190834.

54. Takahashi, T., Nowakowski, R.S., and Caviness, V.S., Jr. (1995). The cell cycle of the pseudostratified ventricular epithelium of the embryonic murine cerebral wall. J. Neurosci. *15*, 6046–6057. https://doi.org/10.1523/JNEUROSCI.15-09-06046.1995.

55. Quinn, J.C., Molinek, M., Martynoga, B.S., Zaki, P.A., Faedo, A., Bulfone, A., Hevner, R.F., West, J.D., and Price, D.J. (2007). Pax6 controls cerebral cortical cell number by regulating exit from the cell cycle and spec-

56. Kawaguchi, A., Ikawa, T., Kasukawa, T., Ueda, H.R., Kurimoto, K., Saitou, M., and Matsuzaki, F. (2008). Single-cell gene profiling defines differential progenitor subclasses in mammalian neurogenesis. Development *135*, 3113–3124. https://doi.org/10.1242/dev.022616.

57. Nelson, B.R., Hodge, R.D., Bedogni, F., and Hevner, R.F. (2013). Dynamic interactions between intermediate neurogenic progenitors and radial glia in embryonic mouse neocortex: potential role in Dll1-Notch signaling. J. Neurosci. *33*, 9122–9139. https://doi.org/10.1523/JNEUROSCI.0791-13.2013.

58. Farkas, L.M., Haffner, C., Giger, T., Khaitovich, P., Nowick, K., Birchmeier, C., Pääbo, S., and Huttner, W.B. (2008). Insulinoma-associated 1 has a panneurogenic role and promotes the generation and expansion of basal progenitors in the developing mouse neocortex. Neuron *60*, 40–55. https://doi.org/10.1016/j.neuron.2008.09.020.

59. Sessa, A., Mao, C.-A., Hadjantonakis, A.-K., Klein, W.H., and Broccoli, V. (2008). Tbr2 directs conversion of radial glia into basal precursors and guides neuronal amplification by indirect neurogenesis in the developing neocortex. Neuron *60*, 56–69. https://doi.org/10.1016/j.neuron.2008.09.028.

60. Britz, O., Mattar, P., Nguyen, L., Langevin, L.-M., Zimmer, C., Alam, S., Guillemot, F., and Schuurmans, C. (2006). A role for proneural genes in the maturation of cortical progenitor cells. Cereb. Cortex *16 (Suppl 1)*, i138–i151. https://doi.org/10.1093/cercor/bhj168.

61. Yang, L., Chan, A.K.N., Miyashita, K., Delaney, C.D., Wang, X., Li, H., Pokharel, S.P., Li, S., Li, M., Xu, X., et al. (2021). High-resolution characterization of gene function using single-cell CRISPR tiling screen. Nat. Commun. *12*, 4063. https://doi.org/10.1038/s41467-021-24324-0.

62. Li, W., Xu, H., Xiao, T., Cong, L., Love, M.I., Zhang, F., Irizarry, R.A., Liu, J.S., Brown, M., and Liu, X.S. (2014). MAGeCK enables robust identification of essential genes from genome-scale CRISPR/Cas9 knockout screens. Genome Biol. *15*, 554. https://doi.org/10.1186/s13059-014-0554-4.

63. Nag, A., Germaniuk-Kurowska, A., Dimri, M., Sassack, M.A., Gurumurthy, C.B., Gao, Q., Dimri, G., Band, H., and Band, V. (2007). An essential role of human Ada3 in p53 acetylation. J. Biol. Chem. *282*, 8812–8820. https://doi.org/10.1074/jbc.M610443200.

64. Nakamura, Y. (1998). ATM: the p53 booster. Nat. Med. *4*, 1231–1232. https://doi.org/10.1038/3207.

65. Turenne, G.A., Paul, P., Laflair, L., and Price, B.D. (2001). Activation of p53 transcriptional activity requires ATM's kinase domain and multiple N-terminal serine residues of p53. Oncogene *20*, 5100–5110. https://doi.org/10.1038/sj.onc.1204665.

66. Li, M., Fang, X., Baker, D.J., Guo, L., Gao, X., Wei, Z., Han, S., van Deursen, J.M., and Zhang, P. (2010). The ATM–p53 pathway suppresses aneuploidy-induced tumorigenesis. Proc. Natl. Acad. Sci. USA *107*, 14188–14193. https://doi.org/10.1073/pnas.1005960107.

67. Macosko, E.Z., Basu, A., Satija, R., Nemesh, J., Shekhar, K., Goldman, M., Tirosh, I., Bialas, A.R., Kamitaki, N., Martersteck, E.M., et al. (2015). Highly Parallel Genome-wide Expression Profiling of Individual Cells Using Nanoliter Droplets. Cell *161*, 1202–1214. https://doi.org/10.1016/j.cell.2015.05.002.

68. Zünd, D., Gruber, A.R., Zavolan, M., and Mühlemann, O. (2013). Translation-dependent displacement of UPF1 from coding sequences causes its enrichment in 3′ UTRs. Nat. Struct. Mol. Biol. *20*, 936–943. https://doi.org/10.1038/nsmb.2635.

69. Lee, S.R., Pratt, G.A., Martinez, F.J., Yeo, G.W., and Lykke-Andersen, J. (2015). Target Discrimination in Nonsense-Mediated mRNA Decay Requires Upf1 ATPase Activity. Mol. Cell *59*, 413–425. https://doi.org/10.1016/j.molcel.2015.06.036.

70. Hurt, J.A., Robertson, A.D., and Burge, C.B. (2013). Global analyses of UPF1 binding and function reveal expanded scope of nonsense-mediated

Neuron
Article

CellPress

mRNA decay. Genome Res. 23, 1636–1650. https://doi.org/10.1101/gr.157354.113.

71. Zhou, Y., Zhou, B., Pache, L., Chang, M., Khodabakhshi, A.H., Tanaseichuk, O., Benner, C., and Chanda, S.K. (2019). Metascape provides a biologist-oriented resource for the analysis of systems-level datasets. Nat. Commun. 10, 1523. https://doi.org/10.1038/s41467-019-09234-6.

72. Abbas, T., and Dutta, A. (2009). p21 in cancer: intricate networks and multiple activities. Nat. Rev. Cancer 9, 400–414. https://doi.org/10.1038/nrc2657.

73. Macleod, K.F., Sherry, N., Hannon, G., Beach, D., Tokino, T., Kinzler, K., Vogelstein, B., and Jacks, T. (1995). p53-dependent and independent expression of p21 during cell growth, differentiation, and DNA damage. Genes Dev. 9, 935–944. https://doi.org/10.1101/gad.9.8.935.

74. Niculescu, A.B., 3rd, Chen, X., Smeets, M., Hengst, L., Prives, C., and Reed, S.I. (1998). Effects of p21(Cip1/Waf1) at both the G1/S and the G2/M cell cycle transitions: pRb is a critical determinant in blocking DNA replication and in preventing endoreduplication. Mol. Cell. Biol. 18, 629–643. https://doi.org/10.1128/MCB.18.1.629.

75. Chrysanthou, S., Flores, J.C., and Dawlaty, M.M. (2022). Tet1 Suppresses p21 to Ensure Proper Cell Cycle Progression in Embryonic Stem Cells. Cells 11, 1366. https://doi.org/10.3390/cells11081366.

76. Sanson, K.R., Hanna, R.E., Hegde, M., Donovan, K.F., Strand, C., Sullender, M.E., Vaimberg, E.W., Goodale, A., Root, D.E., Piccioni, F., and Doench, J.G. (2018). Optimized libraries for CRISPR-Cas9 genetic screens with multiple modalities. Nat. Commun. 9, 5416. https://doi.org/10.1038/s41467-018-07901-8.

77. Yoon, K.-J., Ringeling, F.R., Vissers, C., Jacob, F., Pokrass, M., Jimenez-Cyrus, D., Su, Y., Kim, N.-S., Zhu, Y., Zheng, L., et al. (2017). Temporal Control of Mammalian Cortical Neurogenesis by m6A Methylation. Cell 171, 877–889.e17. https://doi.org/10.1016/j.cell.2017.09.003.

78. Cowen, L.E., and Tang, Y. (2017). Identification of nonsense-mediated mRNA decay pathway as a critical regulator of p53 isoform β. Sci. Rep. 7, 17535. https://doi.org/10.1038/s41598-017-17283-4.

79. Gudikote, J.P., Cascone, T., Poteete, A., Sitthideatphaiboon, P., Wu, Q., Morikawa, N., Zhang, F., Peng, S., Tong, P., Li, L., et al. (2021). Inhibition of nonsense-mediated decay rescues p53β/γ isoform expression and activates the p53 pathway in MDM2-overexpressing and select p53-mutant cancers. J. Biol. Chem. 297, 101163. https://doi.org/10.1016/j.jbc.2021.101163.

80. Inga, A., Storici, F., Darden, T.A., and Resnick, M.A. (2002). Differential transactivation by the p53 transcription factor is highly dependent on p53 level and promoter target sequence. Mol. Cell. Biol. 22, 8612–8625. https://doi.org/10.1128/MCB.22.24.8612-8625.2002.

81. Schlereth, K., Heyl, C., Krampitz, A.-M., Mernberger, M., Finkernagel, F., Scharfe, M., Jarek, M., Leich, E., Rosenwald, A., and Stiewe, T. (2013). Characterization of the p53 cistrome–DNA binding cooperativity dissects p53's tumor suppressor functions. PLoS Genet. 9, e1003726. https://doi.org/10.1371/journal.pgen.1003726.

82. Weinberg, R.L., Veprintsev, D.B., and Fersht, A.R. (2004). Cooperative binding of tetrameric p53 to DNA. J. Mol. Biol. 341, 1145–1159. https://doi.org/10.1016/j.jmb.2004.06.071.

83. Karimian, A., Ahmadi, Y., and Yousefi, B. (2016). Multiple functions of p21 in cell cycle, apoptosis and transcriptional regulation after DNA damage. DNA Repair 42, 63–71. https://doi.org/10.1016/j.dnarep.2016.04.008.

84. Melanson, B.D., Bose, R., Hamill, J.D., Marcellus, K.A., Pan, E.F., and McKay, B.C. (2011). The role of mRNA decay in p53-induced gene expression. RNA 17, 2222–2234. https://doi.org/10.1261/rna.030122.111.

85. Waldman, T., Kinzler, K.W., and Vogelstein, B. (1995). p21 is necessary for the p53-mediated G1 arrest in human cancer cells. Cancer Res. 55, 5187–5190.

86. Barr, A.R., Cooper, S., Heldt, F.S., Butera, F., Stoy, H., Mansfeld, J., Novák, B., and Bakal, C. (2017). DNA damage during S-phase mediates the prolif-eration-quiescence decision in the subsequent G1 via p21 expression. Nat. Commun. 8, 14728. https://doi.org/10.1038/ncomms14728.

87. Engeland, K. (2018). Cell cycle arrest through indirect transcriptional repression by p53: I have a DREAM. Cell Death Differ. 25, 114–132. https://doi.org/10.1038/cdd.2017.172.

88. Le Hir, H., Gatfield, D., Izaurralde, E., and Moore, M.J. (2001). The exon-exon junction complex provides a binding platform for factors involved in mRNA export and nonsense-mediated mRNA decay. EMBO J. 20, 4987–4997. https://doi.org/10.1093/emboj/20.17.4987.

89. Mabin, J.W., Woodward, L.A., Patton, R.D., Yi, Z., Jia, M., Wysocki, V.H., Bundschuh, R., and Singh, G. (2018). The Exon Junction Complex Undergoes a Compositional Switch that Alters mRNP Structure and Nonsense-Mediated mRNA Decay Activity. Cell Rep. 25, 2431–2446.e7. https://doi.org/10.1016/j.celrep.2018.11.046.

90. Silver, D.L., Watkins-Chow, D.E., Schreck, K.C., Pierfelice, T.J., Larson, D.M., Burnetti, A.J., Liaw, H.-J., Myung, K., Walsh, C.A., Gaiano, N., and Pavan, W.J. (2010). The exon junction complex component Magoh controls brain size by regulating neural stem cell division. Nat. Neurosci. 13, 551–558. https://doi.org/10.1038/nn.2527.

91. Mao, H., Pilaz, L.-J., McMahon, J.J., Golzio, C., Wu, D., Shi, L., Katsanis, N., and Silver, D.L. (2015). Rbm8a haploinsufficiency disrupts embryonic cortical development resulting in microcephaly. J. Neurosci. 35, 7003–7018. https://doi.org/10.1523/JNEUROSCI.0018-15.2015.

92. Mao, H., McMahon, J.J., Tsai, Y.-H., Wang, Z., and Silver, D.L. (2016). Haploinsufficiency for Core Exon Junction Complex Components Disrupts Embryonic Neurogenesis and Causes p53-Mediated Microcephaly. PLoS Genet. 12, e1006282. https://doi.org/10.1371/journal.pgen.1006282.

93. McSweeney, C., Dong, F., Chen, M., Vitale, J., Xu, L., Crowley, N., Luscher, B., Zou, D., and Mao, Y. (2020). Full function of exon junction complex factor, Rbm8a, is critical for interneuron development. Transl. Psychiatry 10, 379. https://doi.org/10.1038/s41398-020-01065-0.

94. Pilaz, L.-J., McMahon, J.J., Miller, E.E., Lennox, A.L., Suzuki, A., Salmon, E., and Silver, D.L. (2016). Prolonged Mitosis of Neural Progenitors Alters Cell Fate in the Developing Brain. Neuron 89, 83–99. https://doi.org/10.1016/j.neuron.2015.12.007.

95. Zheng, S., Gray, E.E., Chawla, G., Porse, B.T., O'Dell, T.J., and Black, D.L. (2012). PSD-95 is post-transcriptionally repressed during early neural development by PTBP1 and PTBP2. Nat. Neurosci. 15, 381–388. https://doi.org/10.1038/nn.3026.

96. Lin, L., Zhang, M., Stoilov, P., Chen, L., and Zheng, S. (2020). Developmental Attenuation of Neuronal Apoptosis by Neural-Specific Splicing of Bak1 Microexon. Neuron 107, 1180–1196.e8. https://doi.org/10.1016/j.neuron.2020.06.036.

97. Frappart, P.-O., Tong, W.-M., Demuth, I., Radovanovic, I., Herceg, Z., Aguzzi, A., Digweed, M., and Wang, Z.-Q. (2005). An essential function for NBS1 in the prevention of ataxia and cerebellar defects. Nat. Med. 11, 538–544. https://doi.org/10.1038/nm1228.

98. Whitfield, M.L., Sherlock, G., Saldanha, A.J., Murray, J.I., Ball, C.A., Alexander, K.E., Matese, J.C., Perou, C.M., Hurt, M.M., Brown, P.O., and Botstein, D. (2002). Identification of genes periodically expressed in the human cell cycle and their expression in tumors. Mol. Biol. Cell 13, 1977–2000. https://doi.org/10.1091/mbc.02-02-0030.

99. Blue, S.M., Yee, B.A., Pratt, G.A., Mueller, J.R., Park, S.S., Shishkin, A.A., Starner, A.C., Van Nostrand, E.L., and Yeo, G.W. (2022). Transcriptome-wide identification of RNA-binding protein binding sites using seCLIP-seq. Nat. Protoc. 17, 1223–1265. https://doi.org/10.1038/s41596-022-00680-z.

100. Smith, T., Heger, A., and Sudbery, I. (2017). UMI-tools: modeling sequencing errors in Unique Molecular Identifiers to improve quantification accuracy. Genome Res. 27, 491–499. https://doi.org/10.1101/gr.209601.116.

101. Martin, M. (2011). Cutadapt removes adapter sequences from high-throughput sequencing reads. EMBnet.journal *17*, 10–12. https://doi.org/10.14806/ej.17.1.200.

102. Dobin, A., Davis, C.A., Schlesinger, F., Drenkow, J., Zaleski, C., Jha, S., Batut, P., Chaisson, M., and Gingeras, T.R. (2013). STAR: ultrafast universal RNA-seq aligner. Bioinformatics *29*, 15–21. https://doi.org/10.1093/bioinformatics/bts635.

103. Van Nostrand, E.L., Pratt, G.A., Shishkin, A.A., Gelboin-Burkhart, C., Fang, M.Y., Sundararaman, B., Blue, S.M., Nguyen, T.B., Surka, C., Elkins, K., et al. (2016). Robust transcriptome-wide discovery of RNA-binding protein binding sites with enhanced CLIP (eCLIP). Nat. Methods *13*, 508–514. https://doi.org/10.1038/nmeth.3810.

104. Horlbeck, M.A., Gilbert, L.A., Villalta, J.E., Adamson, B., Pak, R.A., Chen, Y., Fields, A.P., Park, C.Y., Corn, J.E., Kampmann, M., and Weissman, J.S. (2016). Compact and highly active next-generation libraries for CRISPR-mediated gene repression and activation. Elife *5*, e19760. https://doi.org/10.7554/eLife.19760.

105. Liu, Q., Chan, A.K.N., Chang, W.-H., Yang, L., Pokharel, S.P., Miyashita, K., Mattson, N., Xu, X., Li, M., Lu, W., et al. (2022). 3-Ketodihydrosphingosine reductase maintains ER homeostasis and unfolded protein response in leukemia. Leukemia *36*, 100–110. https://doi.org/10.1038/s41375-021-01378-z.

🗗 **CellPress**

STAR★METHODS

KEY RESOURCES TABLE

REAGENT or RESOURCE	SOURCE	IDENTIFIER
Antibodies		
Rabbit anti-UPF2	Jens Lykke-Andersen Lab, UCSD	N/A
Rabbit polyclonal anti-TBR1	Abcam	Cat#ab31940 RRID: AB_2200219
Mouse monoclonal anti-Satb2	Abcam	Cat#ab51502 RRID: AB_882455
Rabbit polyclonal anti-Pax6	BioLegend	Cat#901301 RRID: AB_2749901
Alexa Fluor 488 Mouse anti-Pax6	BD Biosciences	Cat#561664 RRID: AB_10895587
Rabbit polyclonal anti-Ki67	Abcam	Cat#ab66155 RRID: AB_1140752
Rabbit polyclonal anti-TBR2	Abcam	Cat#ab23345 RRID: AB_778267
Rat monoclonal anti-TBR2	Invitrogen	Cat#14-4875-82 RRID: AB_11042577
Rat monoclonal anti-CTIP2	Abcam	Cat#ab18465 RRID: AB_2064130
Rabbit monoclonal anti-NeuN	Cell Signaling Technology	Cat#24307 RRID: AB_2651140
Mouse monoclonal anti-Cre	Millipore Sigma	Cat#MAB3120 RRID: AB_2085748
Rabbit polyclonal anti-cleaved Caspase3	Cell Signaling Technology	Cat#9661 RRID: AB_2341188
Mouse monoclonal anti-NEUROD2	Santa Cruz	Cat#sc-365896 RRID: AB_10843361
Mouse monoclonal anti-GAD67	Millipore Sigma	Cat#MAB5406 RRID: AB_2278725
Chicken polyclonal anti-GFP	Aves Labs	Cat#GFP-1020 RRID: AB_10000240
Rabbit monoclonal anti-p21	Abcam	Cat#ab188224 RRID: AB_2734729
Mouse monoclonal anti-p21	BD Biosciences	Cat#556431 RRID: AB_396415
Mouse monoclonal anti-P53	Cell Signaling Technology	Cat#2524 RRID: AB_331743
Rabbit polyclonal anti-P53	Leica Biosystems	Cat#P53-CM5P RRID: AB_2744683
Mouse monoclonal anti-BrdU	Millipore Sigma	Cat#B8434 RRID: AB_476811
Mouse monoclonal anti-AK1	Santa Cruz	Cat# sc-365316 RRID:AB_10846082
Rabbit monoclonal anti-SESN2	Abcam	Cat# ab178518 RRID:AB_2716805
Mouse monoclonal anti-GAPDH (clone 6C5)	Thermo Fisher Scientific	Cat#AM4300 RRID: AB_2536381
Rabbit monoclonal anti-GAPDH	Cell Signaling Technology	Cat#2118 RRID: AB_561053

(Continued on next page)

Continued

REAGENT or RESOURCE	SOURCE	IDENTIFIER
Goat anti-Rat IgG (H+L) Cross-Adsorbed Secondary Antibody, Alexa Fluor 568	Thermo Fisher Scientific	Cat#A-11077 RRID: AB_2534121
Donkey anti-Rabbit IgG (H+L) Highly Cross-Adsorbed Secondary Antibody, Alexa Fluor 488	Thermo Fisher Scientific	Cat#A-21206 RRID: AB_141708
Donkey anti-Rabbit IgG (H+L) Highly Cross-Adsorbed Secondary Antibody, Alexa Fluor 568	Thermo Fisher Scientific	Cat#A-10042 RRID: AB_2534017
Donkey anti-Mouse IgG (H+L) Highly Cross-Adsorbed Secondary Antibody, Alexa Fluor 568	Thermo Fisher Scientific	Cat#A-10037 RRID: AB_2534013
Donkey anti-Rabbit IgG (H+L) Highly Cross-Adsorbed Secondary Antibody, Alexa Fluor 647	Thermo Fisher Scientific	Cat#A-31573 RRID: AB_2536183
Donkey anti-Mouse IgG (H+L) Highly Cross-Adsorbed Secondary Antibody, Alexa Fluor 647	Thermo Fisher Scientific	Cat#A-31571 RRID: AB_162542
HRP conjugated goat anti-Rabbit secondary antibody	Cell Signaling Technology	Cat#7074 RRID: AB_2099233
HRP conjugated goat anti-Mouse secondary antibody	Cell Signaling Technology	Cat#7076 RRID: AB_330924
Bacterial and virus strains		
NEB 5-alpha competent *E.coli* (high efficiency)	New England Biolabs	Cat#C2987I
FUCGW-Cre-GFP lentivirus	UCLA Vector Core	N/A
GFP lentivirus	UCLA Vector Core	N/A
pCDH-CB-empty backbone lentivirus (Ctrl)	UCLA Vector Core	N/A
pCDH-CB-iCre lentivirus (iCre)	UCLA Vector Core	N/A
pCDH-CB-*Cdkn1a* lentivirus (*Cdkn1a*)	Lab made	N/A
AAV-Cre	pAAV.CMV.HI.eGFP-Cre.WPRE.SV40 (unpublished) was a gift from James M. Wilson (Addgene viral prep # 105545-AAV9)	Cat#105545 RRID: Addgene_105545
AAV-GFP	pAAV.CMV.PI.EGFP.WPRE.bGH (unpublished) was a gift from James M. Wilson (Addgene viral prep # 105530-AAV9)	Cat#105530 RRID: Addgene_105530
Chemicals, peptides, and recombinant proteins		
EdU	Thermo Fisher Sci.	Cat#A10044
BrdU	Millipore Sigma	Cat#19-160
DAPI	Millipore Sigma	Cat#D9542
Animal-Free Recombinant Human EGF	Peprotech	Cat#AF-100-15
Recombinant Human FGF-basic (β-FGF)	Peprotech	Cat#AF-100-18B
1X TrypLE Express	Invitrogen	Cat#12-604-021
DMEM/F12 medium	Gibco	Cat#11320033
B-27 Supplement	Gibco	Cat#17504044
GlutaMAX Supplement	Gibco	Cat#35050061
Poly-L-Ornithine Hydrochloride	Millipore Sigma	Cat#P2533
Fibronectin	Millipore Sigma	Cat#F4759
Albumin, Bovine Fraction V (BSA)	Research Pro. Int.	Cat#A30075
Neurobasal medium	Gibco	Cat#21103049

CellPress

Continued

REAGENT or RESOURCE	SOURCE	IDENTIFIER
Donkey serum	Millipore Sigma	Cat#S30-100ML
Hank's balanced salt solution (HBSS)	Gibco	Cat#14175145
ProLong Gold Antifade Mountant	Thermo Fisher Sci.	Cat#P36930
Benzonase Nuclease	Millipore Sigma	Cat#E1014
TRIzol Reagent	Thermo Fisher Sci.	Cat#15596018
TURBO DNase (2 U/μl)	Thermo Fisher Sci.	Cat#AM2239
M-MLV Reverse Transcriptase	Promega	Cat#M1705
Taq DNA Polymerase with ThermoPol® Buffer	New England Biolabs	Cat#M0267
Phusion Hot Start II DNA Polymerase	Thermo Fisher Sci.	Cat#F549S
cOmplete, EDTA-free Protease Inhibitor Cocktail	Roche	Cat#11873580001
PhosSTOP phosphatase inhibitor tablets	Millipore Sigma	Cat#4906845001
4X Laemmli Sample Buffer	Bio-Rad	Cat#1610747
Coomassie Blue G-250 Stain Solution	Teknova	Cat#C1040
Carprofen	Sigma-Aldrich	Cat#PHR1452
Fast Green FCF Dye	Sigma-Aldrich	Cat#F7252
Penicillin-Streptomycin (10,000 U/mL)	Gibco	Cat#15140122
Actinomycin D	Sigma-Aldrich	Cat#A1410
Polyethylenimine Hcl Max	Fisher Scientific	Cat#NC1038561
Protamine sulfate	MP Biomedicals	Cat#194729
Puromycin	Fisher Scientific	Cat#501414402
Blasticidin S HCl	Thermo Fisher Scientific	Cat#MT30100RB
7-Aminoactinomycin D (7-AAD)	Thermo Fisher Scientific	Cat#A1310
EcoRI-HF restriction enzyme	New England Biolabs	Cat#R3101
BamHI-HF restriction enzyme	New England Biolabs	Cat#R3136
Critical commercial assays		
Click-iT EdU Alexa Fluor 488 Imaging Kit	Thermo Fisher Scientific	Cat#C10337
Click-iT EdU Alexa Fluor 555 Imaging Kit	Thermo Fisher Scientific	Cat#C10338
Click-iT EdU Assay Kit for Flow Cytometry	Thermo Fisher Scientific	Cat#C10425
FITC Annexin V Apoptosis Detection Kit	BD Biosciences	Cat#556547
TruSeq mRNA library prep kit	Illumina	Cat#RS-122-2101
Chromium Next GEM Single Cell 3' GEM, Library & Gel Bead Kit v3.1	10x Genomics	Cat#1000128
EndoFree Plasmid Maxi Kit	Qiagen	Cat#12362
QIAprep Spin Miniprep Kit	Qiagen	Cat#27106
Pierce BCA Protein Assay Kit	Thermo Fisher Scientific	Cat#23227
Power SYBR Green PCR Master Mix	Thermo Fisher Scientific	Cat#4368708
Radiance Plus - ECL Reagent	Azure Biosystems	Cat#AC2103
SuperSignal West Pico PLUS Chemiluminescent Substrate	Thermo Fisher Scientific	Cat#34580
Deposited data		
Upf2 RNA Expression in Mouse	Expression Atlas	ensmusg00000043241
RNA-Seq of Emx1-*Upf2*^{fl/fl} E13.5 mouse cortices	This paper	GSE220460
scRNA-Seq to the CD1 embryonic mouse cortex of E11.5, E13.5, E15.5 and E17.5	Yuzwa et al.[29]	GSE107122
Epigenetic library CRISPRi_screen in mouse *Upf2*^{fl/fl} NPCs	This paper	GSE217735
scRNA-Seq of mouse *Upf2*^{fl/fl} NPCs	This paper	GSE220461

Continued

REAGENT or RESOURCE	SOURCE	IDENTIFIER
UPF1-eCLIP RNA-Seq in mouse *Upf2*^{fl/fl} NPCs	This paper	GSE210437
Bulk RNA-Seq of *Upf2*^{fl/fl} and *Upf2*^{fl/fl} *Trp53*^{fl/fl} NPCs	This paper	GSE220459
snRNA-Seq of Emx1-*Upf2*^{fl/fl} E15.5 mouse cortices	This paper	GSE253825
Experimental models: Cell lines		
HEK 293T cells	A gift from Chen lab	N/A
Upf2^{fl/fl} NPCs	This paper	N/A
Upf2^{fl/fl} *Trp53*^{fl/fl} NPCs	This paper	N/A
Trp53^{fl/fl} NPCs	This paper	N/A
Experimental models: Organisms/strains		
Upf2 loxp/loxp mice	Zheng et al.[95]	N/A
Upf2 Emx1 conditional knockout mice	Lin et al.[96]	N/A
Upf2 Nex conditional knockout mice	This paper	N/A
Upf2 Nestin conditional knockout mice	This paper	N/A
Trp53 loxp/loxp mice	The Jackson Laboratory	Cat#JAX:008462 RRID:IMSR_JAX:008462
C57BL/6 WT mice	The Jackson Laboratory	Cat#JAX:000664 RRID:IMSR_JAX:000664
Oligonucleotides		
Primers for genotyping, see Table S1	This paper	N/A
Primers for RT-qPCR, see Table S1	This paper	N/A
Oligos for shRNA, see Table S1	This paper	N/A
Oligos for sgRNA, see Table S2	This paper	N/A
Recombinant DNA		
pCDH-CB empty backbone	pCDH-CB was a gift from Kazuhiro Oka (unpublished)	Cat#72267 RRID:Addgene_72267
pCDH-CB-iCre	pCDH-CB-iCre was a gift from Kazuhiro Oka (unpublished)	Cat#72257 RRID:Addgene_72257
sgLuc_ipUSEPR lentiviral vector	This paper	N/A
sgTR657_ipUSEPR lentiviral vector	This paper	N/A
pPAX2	pPAX2 was a gift from Didier Trono (unpublished)	Cat#12260 RRID:Addgene_12260
pMD2.G	pMD2.G was a gift from Didier Trono (unpublished)	Cat#12259 RRID:Addgene_12259
ipUSEPR lentiviral sgRNA vector	This paper	N/A
Epigenetic sgRNA library	This paper	N/A
pCAGIG-CDKN1A	This paper	N/A
pCAGIG-shCdkn1a	This paper	N/A
pCDH-CB-Cdkn1a	This paper	N/A
Software and algorithms		
ImageJ	NIH	https://imagej.nih.gov/ij/; RRID: SCR_003070
ImageQuant TL	GE Bio-Sciences	RRID: SCR_014246
NovoExpress software	ACEA Biosciences	https://www.aceabio.com/products/novoexpress-software/; RRID: SCR_024676
NIS-Elements BR4.5 Software	Nikon	http://www.nikoninstruments.com/Products/Software/NIS-Elements-Basic-Research RRID: SCR_002776

(Continued on next page)

Continued

REAGENT or RESOURCE	SOURCE	IDENTIFIER
ZEN Blue	Zeiss	https://www.zeiss.com/microscopy/en/products/software/zeiss-zen.html RRID:SCR_013672
GraphPad Prism 8 software	GraphPad	https://www.graphpad.com/scientific-software/prism/ RRID:SCR_002798
BioRender	BioRender	https://www.biorender.com RRID:SCR_018361
eCLIP-Seq codes	Yeo lab	https://zenodo.org/records/5076591
Custom codes	This paper	https://zenodo.org/records/10899648
Other		
GE Typhoon FLA9000 Biomolecular Imager	GE Bio-Sciences	N/A
ChemiDoc	Bio-Rad	Cat#17001401
ECM 830 Electroporation System	BTX	Cat#45-0052
Varioskan, LUX	Thermo Fisher Scientific	Type 3020
Immobilon-FL PVDF Membrane	Millipore	Cat#IPFL00010
Cytosmart Cell counter	Corning	Cat#6749
NovoCyte Flow Cytometer	ACEA Biosciences	N/A
C1000 Touch Thermal Cycler	Bio-Rad	Cat#1851148
Milli-Q Water Purification System	Millipore	Cat#Z00QSV001
SW41 Ti rotor	Beckman	Cat#331362
Optima L-90K Ultracentrifuge	Beckman	Cat#365672
UV Stratalinker 1800	Stratagene	Cat#400071
Agilent 2100 Bioanalyzer	Agilent Technologies	Cat#G2938B
10x Chromium Controller	10x Genomics	Cat#1000204

RESOURCE AVAILABILITY

Lead contact

Further information and requests for resources and reagents should be directed to and will be fulfilled by the lead contact, Sika Zheng (sika.zheng@ucr.edu).

Materials availability

All the reagents generated in this study are available from the lead contact without restriction or with a completed Materials Transfer Agreement.

Data and code availability

- All the deep-sequencing data have been uploaded to the Gene Expression Omnibus repository. The accession numbers of all sequencing data were listed in key resources table. All non-standardized data will be shared upon request.
- All pipeline code for eCLIP-Seq is available on GitHub at: http://github.com/yeolab/eclip and on Zenodo at: https://zenodo.org/records/5076591, and all other custom codes used in the study is available on GitHub at: https://github.com/NaotoKubota/Neuron_Upf2_2024 and Zenodo at: https://zenodo.org/records/10899648.
- Any additional information required to reanalyze the data reported in this paper is available from the lead contact upon request.

EXPERIMENTAL MODEL AND STUDY PARTICIPANT DETAILS

Animals

Exons 2 and 3 of mouse *Upf2* were targeted by inserting two loxP sites separately in introns 1 and 3 (Figure 1A). This *Upf2*$^{loxp/loxp}$ mouse line was described before.[95] Emx1-Cre$^{+/-}$ (stock number 005628), Nex- Cre$^{+/-}$ (gift from Dr. Iryna Ethell), and Nestin-Cre$^{+/-}$ (stock number 003771) mice were purchased from the Jackson Laboratory and bred with *Upf2*$^{loxp/loxp}$ mice to generate *Upf2* conditional KO mice. *Trp53*$^{loxp/loxp}$ mice (Jackson Laboratory stock number 008462) were used to generate Emx1-Cre$^{+/-}$; *Upf2*$^{loxp/loxp}$; *Trp53*$^{loxp/loxp}$ double conditional KO mice (*Upf2 Trp53*dKO). For time pregnancy, *Upf2*cKO embryos were generated by crossing Emx1- Cre$^{+/-}$; *Upf2*$^{loxp/+}$ males with Emx1-Cre$^{+/+}$; *Upf2*$^{loxp/loxp}$ females, or Nex- Cre$^{+/-}$; *Upf2*$^{loxp/+}$

males with Nex-Cre^{+/+}; *Upf2*[loxp/loxp] females. *Upf2 Trp53*dKO embryos were generated by crossing Emx1- Cre^{+/−}; *Upf2*[loxp/+]; *Trp53*[loxp/loxp] males with Emx1-Cre^{+/+}; *Upf2*[loxp/loxp]; *Trp53*[loxp/loxp] females. Embryonic mice of both sexes from E13 to E17 and newborn mice at P0 were used for *in vivo* studies. The age of P24, 4M and 20M and embryonic day 16 C57BL/6J female and male mice (Jackson Laboratory, stock number 000664) were used. Under the observation, no influence of sex was found in any of those mouse lines. All genotyping primers were listed in Table S1. All mice were maintained and generated for experiments in accordance with the requirements of the Institutional Animal Care and Use Committees (IACUC) at the University of California, Riverside.

Generation of Mouse cortical neural progenitor cells
Primary cortical neurospheres and neural progenitor cell culture were performed as described previously.[97] Mouse neocortices (E14.5) were collected and digested in 1x TrypLE Express (Invitrogen/GIBCO, 12-604-021) at 37 °C for 15 to 20 minutes. Neurospheres were cultured in neural stem cell medium containing DMEM-F12 (Invitrogen/GIBCO, 11320033), 1x B27 (Invitrogen /GIBCO, 17504044), 1x GlutaMAX (Invitrogen/GIBCO, 35050061), 20 ng/ml EGF (Peprotech, AF-100-15) and 20 ng/ml b-FGF (Peprotech, AF-100-18B) for 5 to 7 days in a T25 flask. Then neurospheres were dissociated in 1x TrypLE Express and extendedly cultured in a T75 flask for another 5 to 7 days. After that, neural progenitor cells were plated on dishes or plates and pre-coated with 50 mg/ml polyornithine (Sigma, P2533) and 1 mg/ml fibronectin (Sigma, F4759) for 2 hours at 37 °C. Cortical neural progenitor cells are usually passaged twice or thrice to eliminate the clusters before experiments.

E. coli competent cells
NEB 5-alpha competent E. coli (high efficiency) cells were cultured in LB medium at a 37°C shaker incubator, and LB medium was made by adding 20 g LB Broth (Fisher, BP9722) to 1L of Milli-Q water (adjust pH 7.2) followed by autoclaving for 15 minutes. LB agar plates were made by adding additional 15 g Agar (Fisher, BP1423) in 1 L of LB medium followed by plating 15 mL per 10 cm dishes, and E. coli cells were also cultured in LB agar plates at a 37°C incubator.

METHOD DETAILS

CellTiter-Glo Luminescent Cell Viability Assay
This cell growth assay was performed in primary cortical neurospheres of Nestin-*Upf2*cKO and littermate controls according to the technical bulletin (Promega). After digestion, the cortical NPCs were plated at 15K in 100 μl media per well using 96-well plate (Falcon white flat-bottom TC plate). For each biological replicate, three technical replicates were plated at same time. Meanwhile, three control wells containing medium without cells were plated to obtain a value for background luminescence. Before detection, the plate and its contents were equilibrated at room temperature for around 30 minutes. Then 100 μl CellTiter-Glo reagent was added into each well and the plate was mixed for 2 minutes on an orbit shaker to induce cell lysis. After the plate to incubate at room temperature for additional 10 minutes, Varioskan LUX (Thermo Scientific) was used to detect the luminescent signal at 30°C from 24 hours to 120 hours after cell plating.

Mouse Brain Sectioning and Immunofluorescence Staining
Mouse brains were humanely collected at desired stages and fixed in ice-cold 4% paraformaldehyde (PFA, Acros Organics, AC416785000) for 4-14 hours, depending on embryonic and postnatal stages. Fixed brains were then washed three times with cold PBS (pH7.4), embedded in 3% agarose gel, and sectioned to 50 to 100 μm with Vibratome LEICA VT1000 S (Leica). For staining, brain sections were washed three times with cold 1x PBS, permeabilized with 0.5% Triton X-100 (Electron Microscopy Sciences, 22140) in PBS for half an hour at room temperature, and immersed in blocking buffer (10% donkey serum, 0.5% BSA, 0.3% Triton X-100 in pH 7.4 PBS) for an hour. Afterwards, the sections were incubated with primary antibodies diluted in the blocking buffer at 4 °C overnight. The primary antibodies were used as follows: rabbit anti-TBR1 (Abcam#ab31940, 1:400), mouse anti-SATB2 (Abcam#ab51502, 1:400), rabbit anti-PAX6 (BioLegend#901301, 1:400), mouse anti-PAX6 (BD Biosciences#561664, 1:100), rabbit anti-Ki67 (Abcam#ab66155, 1:400), rabbit anti-TBR2 (Abcam#ab23345, 1:400), rat anti-TBR2 (Invitrogen#14-4875-82, 1:200), rat anti-CTIP2 (Abcam#ab18465, 1:400), rabbit anti-p21 (Abcam#ab188224, 1:400). Then, brain sections were rinsed three times with PBS containing 0.3% Triton X-100 and incubated with appropriate Alexa Fluor conjugated secondary antibodies (Thermo Fisher Scientific, 1:1000) at 4 °C overnight on the second day. The next day, nuclei were visualized by incubating for 30 min with 0.2 μg/ml 4,6-diamidino-2-phenylindole (DAPI, Sigma, D9542) in PBS at room temperature. After three rounds of washing, stained sections were mounted with ProLong Gold Antifade Mountant (Thermo Fisher Scientific, P36930).

Mouse NPCs lentivirus infection and growth curve test
400k *Upf2*^{fl/fl}, *Trp53*^{fl/fl} or *Upf2*^{fl/fl} *Trp53*^{fl/fl} NPCs were plated into one well of pre-coated 12-well plates and allowed to grow overnight. No lentivirus (Mock) 10 μl GFP-LV (UCLA Vector Core, GFP) or FUCGW-Cre (UCLA Vector Core, Cre-LV, Cre) were added to 500 μl NPC media with 4 μg/ml protamine sulfate (MP Biomedicals, 194729) for 24 hours. 24 hours after the infection, NPCs were dissociated with 1x TrypLE Express and replated with 200k NPCs per well to pre-coated 6 well plates. One well of NPCs was dissociated and counted every 24 to 120 hours after infection.

RNA purification and quantitative RT-PCR analysis

1 ml of TRIzol (Thermo Fisher, 15596018) was directly added to the cells or cortex tissue to extract total RNA following the manufacturer protocol. DNase treatment was performed at 37 °C for 35 min to degrade residue genomic DNA after TRIzol RNA isolation with 1 unit of Turbo DNase (Thermo Fisher., AM2239) per 10 μg total RNA. Following the DNase treatment, RNA was purified again using phenol-chloroform pH 4.5 (VWR, 97064-744). RNA concentrations were measured using a Nanodrop 2000c. cDNA was synthesized using 1 μg of DNA-free total RNA. The reverse transcription used 1 μl of 30 μM random hexamers (IDT) and 200 units of Promega M-MLV reverse transcriptase (Promega, M1705) in a 20 μl reaction following the Promega protocol. The completed 20 μl cDNA reactions were diluted with 180 μl of nuclease-free H_2O (1:9) as the working concentration. RT-qPCR experiments were performed using a 2x Power SYBR Green PCR master mix (Thermo Fisher, 4368708), following the manufacturer's protocol. A 10 μl reaction consisted of 5 μl 2x Power SYBR Green PCR master mix, 0.3 μl of 10 μM forward primer, 0.3 μl of 10 μM reverse primer, and 3 μl of cDNA. A QuantStudio 6 Real-Time PCR instrument (Thermo Fisher) was used for the RT-qPCR assay. The run program was as follows: 50 °C for 2 min, 95 °C for 15 s, and 60 °C for 1 min, with the 95 °C and 60 °C steps repeated for 40 cycles. A melting curve test from 60 °C to 95 °C at a 0.05 °C/s measuring rate was performed after each run for quantity control. All primers were listed in Table S1.

EdU and BrdU Labeling

Cumulative EdU labeling was performed by intraperitoneal injections of 50 mg/kg EdU (Invitrogen, A10044) in sterile PBS into E14.5 or E15.5 pregnant mice, repeated at 3 hours intervals up to 24 hours. Then E15.5 pregnant mice were collected at the expected time points indicated in Figure 3. Before dissection, all embryos were transferred to ice-cold 1x Hank's balanced salt solution (HBSS, Gibco, 14175145) to stop further incorporation of EdU.

For EdU labeling of 24 hours to test the cell cycle exit, timed pregnant mice were injected intraperitoneally at E14.5 with 100 mg/kg EdU in sterile PBS and then collected 24 hours later. For EdU labeling of three days, timed pregnant mice were injected at E14.5 with 100 mg/kg EdU in sterile PBS and then collected at E17.5. For BrdU (Millipore Sigma, F4759) labeling of 1.5 hours, timed pregnant mice at E17.5 were injected with 50 mg/kg BrdU and collected at a defined time point before euthanasia. The embryo-containing uteri were transferred immediately to ice-cold HBSS to stop further incorporation of EdU or BrdU. Mouse anti-BrdU (Millipore Sigma#B8434, 1:1000) was used in BrdU immunostaining after the 2M hydrochloric acid (Thermo Fisher, S25358) treatment for 1 hour at room temperature. The staining steps were the same as described before in immunofluorescence staining section.

EdU Staining and Confocal Imaging

After cumulative EdU labeling, E15.5 mouse brains were dissected and fixed with ice-cold 4% PFA for 8 to 10 hours. Vibratome sections (50–100 μm) were used to detect the incorporated EdU with the Click-iT EdU Alexa Fluor 488 Imaging Kit (Thermo Fisher Scientific, C10337). According to the manufacturer's protocol, thick floating sections were modified as follows: 30 minutes for each washing and permeabilization, 60 minutes for Click-iT reaction cocktail incubation, and 90 minutes for the serum blocking. Prior to imaging, the sections were incubated with primary antibodies such as rabbit anti-PAX6 (BioLegend#901301, 1:400) and rat anti-TBR2 (Invitrogen#14-4875-82, 1:200) at 4 °C overnight, followed by secondary antibodies as Alexa Fluor 647 donkey anti-rabbit (Thermo Fisher Scientific, A-315731:1000) and Alexa Fluor 568 goat anti-rat (Thermo Fisher Scientific, A-11077, 1:1000) at 4 °C overnight. The following day, DAPI stained sections were mounted and ready for the confocal imaging and analysis on Zeiss LSM800 with ZEN Blue software.

Analysis of Cell-cycle Parameters

For the analysis of the RGC population, total RGCs were labeled by PAX6$^+$TBR2$^-$ and proliferative RGCs during the EdU labeling period were labeled by EdU$^+$PAX6$^+$TBR2$^-$. For the analysis of the IPC population, total IPCs were labeled by PAX6$^-$TBR2$^+$ and proliferative IPCs during the EdU labeling period were labeled by EdU$^+$PAX6$^-$TBR2$^+$. The proportional values of EdU$^+$ nuclei (EdU$^+$PAX6$^+$TBR2$^-$/PAX6$^+$TBR2$^-$ or EdU$^+$PAX6$^-$TBR2$^+$/PAX6$^-$TBR2$^+$) acquired after the various times of cumulative labeling were used to determine the following cell cycle parameters according to the Excel sheet published by Dr. R. Nowakowski[53]: the growth fraction (representing the total proportion of cycling progenitors, or P), $T_C - T_S$ (the time to reach the growth fraction) and $P*T_S/T_C$ (the proportion of proliferating cells labeled by first EdU injection), from which the T_C and T_S were calculated out.

In Utero Electroporation

In utero electroporation was performed as described previously.[96] Briefly, timed-pregnant *Upf2*$^{fl/+}$;*Emx1*$^+$ mice at E14.5 were anesthetized by isoflurane and the uterine horns were taken out after intraperitoneal injection of 5 mg/kg Carprofen (Sigma). Approximately 1-1.5 μg endo-free pCAGIG plasmid mixed with 0.05% Fast Green Dye (Sigma) was microinjected into the lateral ventricles of embryos using calibrated micropipettes (VWR International). Five pulses (42V, a duration of 50ms with a 950ms interval) were delivered parallel to the embryonic anteroposterior axis with forceps-type electrodes. Afterwards, the uterus was taken back in the abdominal cavity and the wound was sutured. The mouse embryos were collected two days later at E16.5 for staining and analysis. For CDKN1A overexpression *in vivo*, 1-2 μl pCAGIG-CDKN1A or pCAGIG plasmid (1 μg/μl) was delivered into the C57BL/6 wildtype embryos at E14.5. Then one day later the operated mouse was injected intraperitoneally with 50 mg/kg EdU for 1.5 hours before collecting all embryos. For CDKN1A knockdown *in vivo*, 1-2 μg pCAGIG-shRNA against mouse *Cdkn1a* was delivered into the

Emx1-*Upf2*cKO embryos at E14.5, and then the *Upf2*cKO embryos were collected two days later at E16.5 after the EdU labeling for 1.5 hours as mentioned before. All embryonic brains were collected and fixed with 4% paraformaldehyde in PBS overnight at 4°C for further staining and analysis. All animal surgeries were performed in accordance with the protocol approved by the Institutional Animal Care and Use Committees (IACUC) at the University of California, Riverside.

RNA Sequencing Libraries Construction

RNA samples for library generation were collected from AAV9-GFP-Cre (Addgene, 105545) induced *Upf2*KO NPCs and E14.5 Emx1-Cre *Upf2*fl/fl mouse cortex. For NPCs samples, 200k *Upf2*fl/fl or *Upf2*fl/fl *Trp53*fl/fl NPCs per well were plated in a pre-coated 6-well plate. The mock group was set to add the same volume of NPC media, while the Cre group was added with a MOI= 400k in 1 ml NPC media. 14 hours after the plate and infection, AAV9-contained media was removed and replaced with 2 ml fresh NPC media. 72 hours after the infection, media was removed from the well and 1 ml TRIzol was added to each well for RNA extraction and DNase treatment. Mouse cortex samples were collected from E14.5 Emx1-Cre *Upf2*fl/fl mouse cortex and proceeded to RNA extraction as previously described. All samples passed the QC test in the bioanalyzer analysis with a RIN of at least 9.0.

RNA-Seq libraries were constructed using Illumina TruSeq Stranded Total RNA LT Sample Prep kits (Illumina, RS-122-2101) according to the manufacturer protocol. In brief, 2 μg total RNA per sample was input for library construction. Ribosomal RNA and other non-messenger RNAs were depleted with RNA purification beads, and mRNA was fragmented for first-strand cDNA synthesis. After synthesizing the second strand cDNA, the 3' end of the dsDNA fragments was adenylated and ready to ligate the individual adaptor index. DNA fragments were further enriched with 15 PCR cycles using a PCR primer cocktail. QC tests were performed to verify the fragments' size range from 200 to 650bp. Samples with different indices were multiplexed with the same mass before sending for sequencing.

RNA-Seq Analysis

All premade RNA-Seq libraries were sent for sequencing with the HiSeq 4000 platform. Around 150G raw data per lane was obtained for further analysis. Detailed raw reads number of each sample were listed in Table S6. The raw data were mapped using STAR. The gene-level read counts for gene g are $\{X_{g,1}, X_{g,2}, \ldots, X_{g,n_x}\}$ under condition 1, and $\{Y_{g,1}, Y_{g,2}, \ldots, Y_{g,n_y}\}$ under condition 2, where n_x and n_y are the sample sizes for the two conditions. To identify differentially expressed (DE) genes, we aggregate reads across samples under the same conditions: $X_g = \sum_{k=1}^{n_x} X_{g,k}$ and $Y_g = \sum_{k=1}^{n_y} Y_{g,k}$. Assuming that:

$X_g | (X_g + Y_g = m) \sim$ binomial distribution (m, p), where $p = c_x \theta_{g,x}/(c_x \theta_{g,x} + c_y \theta_{g,y})$; $\theta_{g,x}$ and $\theta_{g,y}$ are the mean expression levels under conditions 1 and 2 respectively; c_x and c_y are the normalization factors. For example, the normalization factor for sample k under condition 1 is calculated as:

$$c_{x,k} = median_{g \in G} \left\{ \frac{X_{g,k}}{exp\left(\left(\sum_{r=1}^{n_x} log(X_{g,r}+1) + \sum_{r=1}^{n_y} log(Y_{g,r}+1)\right) \middle/ (n_x+n_y)\right) - 1} \right\},$$

where the denominator is the geometric mean of gene-level read counts across all samples under both conditions (1 is added to avoid zeros, and then subtracted from the final geometric mean). The final normalization factors for the two conditions are: $c_x = \sum_{k=1}^{n_x} c_{x,k}$ and $c_y = \sum_{k=1}^{n_y} c_{y,k}$. Under the null hypothesis: $\theta_{g,x}/\theta_{g,y} = d$. Then $p = c_x d/(c_x d + c_y)$. Calculate the following probabilities:

$$P_{g,1} = P_{\theta_{g,x}/\theta_{g,y} = 1.5}(X_g + Y_g = m),$$

$$P_{g,2} = P_{\theta_{g,x}/\theta_{g,y} = 1/1.5}(X_g + Y_g = m),$$

Then the p-value for the 2-fold DE change detection (d=2 or 1/2) is $min(1, 2 \times min(P_{g,1}, P_{g,2}))$. The multiple correction was performed on all the 55,573 genes. The adjustment was on all the p-values obtained from the Binomial test aggregating all reads from replicates without any gene filtering step. The false discovery rate (FDR) is controlled at 0.05. To select DEG for downstream analysis, we further required the raw pooled gene-level count should be ≥ 50 and the average TPM ≥ 1 for at least one condition.

Isolation of single nuclei from embryonic cortices for snRNA-Seq

The E15.5 embryonic cortex tissues were dissected out and transferred to a new 15 ml conical tube along with HEB medium (Hibernate A medium containing 1x B27 and 1x GlutaMAX) to cover the tissues. The nuclei isolation was performed according to the 10x Genomics protocol (CG000124). In brief, tissue was incubated on ice in 3 ml chilled lysis buffer (10 mM Tris-HCl, 10 mM NaCl, 3 mM MgCl2 and 0.1% Nonidet P40 Substitute) for 4 minutes. Then, 3 ml chilled HEB medium was added to the lysed cells and mixed with the fire polished silanized Pasteur pipette for around 20 passes. 30 μm MACS SmartStrainer was used to remove cell debris and large clumps. Next, we centrifuged at 500 rcf for 5 min at 4°C and removed the supernatant without disrupting the nuclei pellet. 3 ml Nuclei Wash and Resuspension Buffer (1x PBS with 1.0% BSA and 0.2 U/μl RNase inhibitor) was used twice to wash the isolated nuclei. Finally, we centrifuged at 500 rcf for 5 min at 4°C and resuspended in Nuclei Wash and Resuspension Buffer to a final concentration of 1200 nuclei per μl in WT and 900 nuclei per μl in Emx1-*Upf2*cKO.

Neuron
Article

CellPress

Single cell/single nuclei RNA Sequencing Libraries Construction

NPCs were infected with GFP-LV or Cre-LV, as previously described. 72 hours after the infection, NPCs were dissociated with 1x TrypLE Express and resuspended in 1x PBS with 0.04% BSA (Research Pro. Int., A30075). Concentration and viability tests of GFP and Cre groups were carried out for both groups, and GFP had 715k NPCs/ml with 91.5% viability, while Cre had 552k NPCs/ml with 93.2% viability.

Upf2^{fl/fl} NPCs with GFP-LV and Cre-LV infection or single nuclei isolated from embryonic cortices were used for single-cell library construction (10x Genomics, 1000128). NPCs or single nuclei were loaded into the single-cell chip with a target recovery of 10k cells into the 10x Genomic Chromium machine. After the 10x program finished, 100 μl GEMs per sample were recovered for GEM-RT incubation. GEM-RT cDNA was further cleaned up and amplified with 12 cycles. Samples were determined as passing the QC with fragments ranging from 300 to 9,000bp. 20 μl cDNA per sample was used as input for library generation. After the cDNA fragmentation, end repair, and A-tailing, the adapter was ligated for amplification. Different sample indices (indices from 10x index plate or indices synthesized by IDT) were used for additional 14 PCR cycles. PCR products were cleaned up and size selected, and samples were determined to pass the QC with a size range from 300 to 600bp. Samples with the same mass were multiplexed and sent for sequencing.

Single-cell RNA-Seq Analysis

ScRNA-Seq libraries were sequenced on the HiSeq 4000 platform. Around 150G raw data per lane was obtained. Detailed raw reads number of each sample were listed in Table S6. Cell Ranger (version 5.0.1, reference genome: mm10-2020-A<based on Gencode vM23, and filtering out pseudogenes, TEC, miRNA etc., a total of 32285 genes) was used to perform alignment, filtering, barcode counting, and UMI counting for single-cell RNA-Seq. Cell-cycle-phase-specific marker genes (M/G1, G1/S, S, G2, and G2/M) were obtained from Whitfield et al.[98] Since this study was based on microarray mRNA expression profiling of HeLa cells, gene microarray probes were converted to Ensembl genes according to the reported NCBI gene (Entrezgene) IDs. Genes with probes assigned to different phases were removed. Then these human genes were converted to mouse genes according to the "one-to-one" ortholog information between humans and mice. The cell-cycle genes underwent two filtering steps to remove those that were identified as phase-specific in HeLa but did not correlate well in our NPC samples: (1) only retain genes exhibiting a positive average correlation with other genes in the same phase; (2) retain genes exhibiting a larger mean correlation with other genes within the same phase than the correlation with genes from different phases. For each phase, we averaged the normalized expression levels ($\log_2(CPM+1)$) of the marker genes to define the phase-specific scores of each cell. These scores were then subjected to two normalization steps as previously described.[67] First, for each phase, the scores were Z-transformed across cells. Second, the normalized scores of each cell were further Z-transformed. The scRNA-Seq data (gene-level UMI counts) for RGCs and IPCs were downloaded from the GEO website (GSE107122), in which about 19 thousand Ensembl mouse genes were given gene expression values.

The differential expression (DE) analysis for genes between two groups of cells was performed by the Binomial distribution-based conditional test on the aggregated read counts, targeting a fold change of at least 1.5. The normalization factor was calculated as each sample's total UMI count. The Bonferroni corrected P-value (or FDR in the analysis of RGCs and IPCs) for the differential expression should be ≤ 0.05. To make sure the DE signal was still significant with the consideration of cell-to-cell variation within the same group, we conducted an additional t-test on the cells with at least one UMI ($\log_2(CPM)$, at least five cells with UMI for each group) and required the Bonferroni corrected P-value (or original P in the analysis of RGCs and IPCs) ≤ 0.05. We further required the raw pooled UMI count should be ≥ 50 and the corresponding CPM ≥ 1 for at least one condition. Selected genes represent those passing the above threshold in both replicates (DEfmn_10x and DEfmn_IDT).

Apoptotic analysis for *Upf2*KO NPCs by flow cytometry

Annexin V: FITC Apoptosis Detection Kit I (BD Biosciences, 556547) was used for apoptotic analysis following the manufacturer's protocol. In brief, the same mouse NPCs lentivirus infection protocol as the growth curve test was adopted. With the exception that 10 μl empty backbone-LV (UCLA Vector Core) were used for Ctrl group infection and 10 μl iCre-LV (UCLA Vector Core, iCre) were used as *Upf2*KO group. 72 hours after the infection, NPCs were dissociated and cells were resuspended in the 1x binding buffer with a concentration of 1×10^6 cells/ml. 100 μl NPCs per group were stained with 1 μl 7-AAD (Thermo Fisher, A1310, 1 mg/ml) and 1 μl Annexin V at room temperature for 20 min in the dark. Additional 200 μl 1x binding buffer was added to all samples, and samples were filtered with 5 ml FACS tubes before FACS analysis using NovoCyte Flow Cytometer (ACEA Biosciences).

Analysis of cell cycle progression by EdU pulse labeling

Click-iT™ EdU Alexa Fluor™ 488 Flow Cytometry Assay Kit (Thermo Fisher, C10425) was used for cell cycle progression analysis. *Upf2*^{fl/fl}, *Upf2*^{fl/fl} *Trp53*^{fl/fl} and *Upf2*^{fl/fl}-sgRNA stable expressed NPC lines were used for cell cycle analysis using the same NPC infection protocol as the apoptosis analysis. As for cell cycle analysis with lentiviral *Cdkn1a* overexpression, 10 μl iCre-LV were replaced with 25 μl *Cdkn1a*-LV (lab made) to achieve a similar upregulation of *Cdkn1a* as *Upf2*KO. 72 hours after the infection, 10 μM EdU was added to one well of each group and incubated for a 30 min pulse labeling. All wells were washed with warm 1x PBS and dissociated with 1x TrypLE Express. After centrifuge, NPCs were washed in the cold 1x PBS with 1% BSA and resuspended in the fixative buffer at a concentration of 1×10^6 cells/ml and fixed at 4 °C overnight. The next morning, NPCs were washed cold 1x PBS with 1% BSA and resuspended in 1x Click-iT saponin-based permeabilization and wash reagent at a concentration of 1×10^6 cells/ml. NPCs were

incubated in the permeabilization buffer for 15 min. Transfer 50 μl cell suspension to 250 μl Click-iT reaction cocktail (219 μl 1x PBS, 5 μl CuSO$_4$, 1.25 μl fluorescent dye azide, 25 μl reaction buffer additive) and at room temperature for 30 min in the dark. Cells were washed again with 1x Click-iT saponin-based permeabilization and wash reagent. The DNA content was stained with 1 μl 7-AAD (1 mg/ml) according to the apoptosis protocol and proceeded to the FACS analysis using NovoCyte Flow Cytometer (ACEA Biosciences).

Enhanced UPF1 CLIP analysis

The protocol we used was in line with the nature protocol published by Yeo lab.[99] In brief, 40 million NPCs were dissociated and re-suspended with 4 ml pre-cold 1x PBS in a 10 cm dish. Place the 10 cm dish on the chilled metal plate with the lid removed and cross-linked the samples with UV Stratalinker with 400 mJ/cm^2. All NPCs were collected and centrifuged, and the pellet was flash frozen with liquid nitrogen and stored at −80 °C or dry ice until use. Cell pellets were lysed and sonicated in eCLIP lysis buffer (50 mM Tris-HCl pH 7.4, 100 mM NaCl, 1% NP-40, 0.1% SDS, 0.5% sodium deoxycholate, 1:200 Protease Inhibitor Cocktail III, in RNase/DNase free H$_2$O). RNA was fragmented using RNase I (Ambion) and UPF1: RNA complexes were immunoprecipitated overnight at 4 °C using Dynabeads bound to 2 μg of UPF1-specific antibody (A301-902A). Libraries were also generated from size-matched input (SMInput) samples representing RNAs from whole cell lysates. The UPF1 IPs were subject to a series of washes (high salt wash buffer: 50 mM Tris-HCl pH 7.4, 1 M NaCl, 1 mM EDTA, 1% NP-40, 0.1% SDS, 0.5% sodium deoxycholate, in RNase/DNase-free H$_2$O; wash buffer: 20 mM Tris-HCl pH 7.4, 10 mM MgCl$_2$, 0.2% Tween-20, in RNase/DNase-free H$_2$O) followed by FastAP (Thermo Fisher Scientific) and T4 PNK (NEB) treatment to dephosphorylate the RNA. An adaptor was then ligated to the 3' ends of the dephosphorylated RNAs using T4 RNA Ligase 1 (NEB) and UPF1: RNA complexes were separated via gel electrophoresis and transferred to nitrocellulose membranes. RNA molecules were extracted using Proteinase K (NEB) and SMInput RNA was dephosphorylated and then 3' adaptor-ligated. All samples were reverse transcribed using Superscript III (Invitrogen) and treated with ExoSAP-IT (Affymetrix) to remove free primers and unincorporated dNTPs. A DNA adaptor was then ligated to the 3' ends of the cDNA with T4 RNA Ligase 1 prior to qPCR quantification and PCR amplification using Q5 High-Fidelity 2x Master Mix (NEB). Purified libraries were then sequenced by Illumina sequencing.

eCLIP reads were processed and trimmed of their unique molecular identifiers and adapters using umi_tools (1.0.0) and cutadapt (1.14) respectively.[100,101] Then, rRNA and repeat element filtering was performed by mapping trimmed reads to RepBase with STAR (2.7.6).[102] Surviving reads were mapped to the mouse genome (mm10) and duplicates were removed. Enriched clusters of reads (peaks) from the IP dataset were called using CLIPper. Within each peak, reads from each IP were compared to reads from corresponding size-matched input controls to calculate fold enrichment. Peaks were annotated using Mouse Gencode v15. To quantitatively determine UPF1 binding sites, we used the binding signal enrichment ratio (RPM$_{IP}$/RPM$_{Input}$) across 3'UTRs since the majority of peaks lay within the 3'UTR. We defined transcripts as high-confidence UPF1 binding genes when the ratio was > 8 [log$_2$(fold change) > 3] and p-value < 10^{-5} [Fisher/Chi-square test] (Figure 6D).[103]

Protein extraction and immunoblotting

All protein samples were extracted with standard RIPA buffer with 50 mM Tris-HCl pH 7.4, 150 mM NaCl, 1% Triton X-100, 0.1% SDS, 0.2 μl/ml Benzonase Nuclease (EMD Millipore, E1014) and 1x EDTA-free protease inhibitor cocktail (Roche, 11873580001). For NPC samples, cells were washed with cold 1x PBS twice in the 6-well plate. 100 μl of RIPA buffer per well was added, and NPCs were scrapped to the buffer and then transferred to 1.5 ml Eppendorf tubes. All tubes were rotated at 4 °C for 1 hour to facilitate the lysis process. Samples were centrifuged at 4 °C for 12,000 rpm, 10 minutes, and all supernatants were transferred to new tubes. For brain tissues, protein lysis was shaken up and down at 4 °C for 1 hour and then collected by centrifuging at 14,800 rpm for 20 minutes at 4 °C to get rid of the insoluble residues. Protein concentrations were determined with a BCA kit.

About 20 to 40 μg total protein per sample was loaded to 12% or 4%–12% SDS-PAGE gels for immunoblotting analysis. With electro-separated proteins transferred to PVDF membranes, target proteins were probed with primary antibodies in 1x TBST with 5% BSA. Incubated overnight and detected with appropriate Alexa Fluor (Thermo Fisher, 1:1000) or HRP conjugated (Cell Signaling Technology, 1:5000) secondary antibodies. Images were collected with Typhoon FLA9000 Biomolecular Imager (GE Bio-Sciences) or ChemiDoc (Bio-Rad, 17001401). The intensities of target bands were quantified with the ImageQuant software (GE Bio-Sciences). The primary antibodies were used as follows: rabbit anti-UPF2 (gift from Dr. Jens Lykke-Andersen, 1:1000), mouse anti-CDKN1A (BD Biosciences#556431, 1:1000), rabbit anti-TRP53 (Leica Biosystems#P53-CM5P, 1:500), mouse anti-GAPDH (Thermo fisher#AM4300, clone 6C5, 1:2000), rabbit anti-GAPDH (Cell Signaling Technology #2118, 1;2000).

Half-life measurement of *Cdkn1a* mRNA in mouse NPCs

NPCs were infected with Ctrl or iCre lentivirus following the previous procedure. 72 hours after the infection, different groups of NPCs were treated with 5 μg/ml Actinomycin D (Sigma, A1410) for the indicated time. Cells were collected at 0 hour, followed by 1, 2, 4, 6, and 8 hour(s) by adding 1 ml TRIzol. With the RNA purification and RT-qPCR analysis, the percentage of *Cdkn1a* left relative to 0 hour were determined. Take a log$_{10}$ of these percentages and plot them against time. Linear regression of all collected points, and the decay rate is the minus slope. The half-life could be calculated with 0.301/the decay rate.

Neuron
Article

CellPress

Lentivirus production with HEK 293T cells

All batches of lentivirus were produced with target plasmid or library plasmid with the pPAX2 (Addgene, 12260) and pMD2.G (Addgene, 12259) packaging plasmids. In brief, 3.4x 10^6 293T cells were plated into one 10 cm dish. The next morning, two mixtures were made for the transfection. Mixture 1 contained 5.6 μg pPAX2, 5.6 μg pMD2 and 5.6 μg target plasmid in 420 μl 150 mM NaCl, while mixture 2 contained 51 μl PEI (40 KD, Fisher Scientific, NC1038561) in 204 μl 150 mM NaCl. Mixture 2 was added to mixture 1 and vortex mixed as the transfection mixture. The final mixture was incubated for 10 minutes before adding to 10 ml culture media. 24 hours after the transfection, PEI-containing media was replaced with 10 ml fresh media. Harvest two batches of viral media at 48 and 96 hours after the transfection. Then, media were combined and centrifuged at 2,000 g for 10 min to remove cell debris. All supernatants should be filtered with a 0.45 μm filter and centrifuged at 4 °C for 100,000 g, 2 hours. Carefully remove all supernatants and resuspend the pellet with pre-cold 1x PBS (V1x PBS/Vviral media = 1/200). Storage all concentrated lentivirus at −80 °C until use.

Construction of *Upf2*^fl/fl^-NPC-dCas9-Krab cells

dCas9-Krab lentivirus was delivered to *Upf2*^fl/fl^ NPCs following the previously described protocol. 24 hours after the infection, NPCs from the non-infection control wells and infected wells were seeded into one 10 cm dish each. 48 hours after the infection, all dishes were treated with 1 μg/ml blasticidin (Thermo Fisher, MT30100RB) selection drug. With the complete cell death of the non-infection group, NPCs left in the infected group should be dCas9-Krab positive. Replace with fresh blasticidin containing NPC complete media every 48 hours to remove dead cells until NPCs reach full confluency. NPCs infected with different dosages of lentivirus were collected for the CRISPRi efficiency test.

Briefly, NPC or NPC-dCas9 cells were infected with the same dosage of sgLuciferase or sgRFP at a ∼15% infection rate. 72 hours after the infection, NPCs were dissociated with 1x TrypLE Express, then washed and resuspended with 1x PBS. NPCs were proceeded to FACS analysis to detect the percentage of RFP⁺ cells. CRISPRi efficiency was calculated as below:

$$Ratio_{RFP/Luci} = \frac{Percentage_{NPC\_sgRNA\_RFP} - Percentage_{NPC\_non\_sgRNA}}{Percentage_{NPC\_sgRNA\_Luci} - Percentage_{NPC\_non\_sgRNA}}$$

$$Efficiency = 1 - \frac{Percentage_{NPC\_dCas9\_Krab\_RFP} - Percentage_{NPC\_dCas9\_Krab\_non\_sgRNA}}{Ratio_{RFP/Luci} \times \left(Percentage_{NPC\_dCas9\_sgRNA\_Luci} - Percentage_{NPC\_dCas9\_Krab\_non\_sgRNA}\right)}$$

Two NPC-dCas9-Krab cell lines with the highest CRISPRi efficiency were selected for CRISPRi screening (NPC-dCas9-Krab#5 with 78.8% and NPC-dCas9-Krab#50 with 74.6% KD efficiency).

Epigenetic CRISPR interference (CRISPRi) library screen

For the epigenetics-focused CRISPRi library (Table S2), 3,630 sgRNA sequences targeting the TSS of 720 epigenetic-related genes were designed using the mouse genome-wide CRISPRi-v2.[104] Briefly, guide RNA oligos were synthesized by microarray (Custom Array) and cloned into the ipUSEPR lentiviral vector (hU6-driven sgRNA co-expressed with EF-1a-driven red fluorescent protein [RFP] and puromycin-resistance gene) using the BsmBI (NEB) restriction sites.[61,105] Lentivirus was produced in HEK293 cells by co-transfecting the CRISPRi library plasmid with the pPAX2 and pMD2.G plasmids. The library was then delivered into the NPC-dCas9-Krab cells via lentiviral transduction. Briefly, cells were infected with the library at ∼15% infection (monitored by flow cytometry for RFP expression; 2 replicates each condition) and selected by 1 μg/ml puromycin (Fisher Scientific, 501414402). 3.6 million cells from each replicate were collected as the Mock group. NPC-dCas9-Krab-sgRNA⁺ cells were then infected with GFP or Cre lentivirus as previously described. An additional MOI=400k AAV9-GFP (Addgene, 105530) or AAV9-Cre was added to keep the *Upf2*KO pressure at 48 hours post infection. 72 hours after the lentivirus infection, AAV9-containing media was replaced with fresh NPC media. 120 hours after infection, NPCs were dissociated and counted (Replicate#1: GFP: 13.5 million, Cre: 2 million; Replicate#2: GFP: 17.7 million, Cre: 2 million) for sgRNA detection. The integrated sgRNA in each sample was PCR-amplified from genomic DNA (NEB, NEBNext Ultra II Q5) using primers DCF01 5'-CTTGTGGAAAGGACGAAACACCG-3' and DCR03 5'- CCTAGGAACAGCGGTTT AAAAAAGC-3' for high-throughput sequencing (NextSeq550, Illumina). To quantify sgRNA reads, nucleotide sequences that matched the sgRNA backbone structure (5'-CACCG and GTTT-3') were extracted and mapped to the library sgRNA sequences using Bowtie2 and then analyzed using the Model-based Analysis of Genome-wide CRISPR-Cas9 Knockout (MAGeCK v0.5.9.3) algorithm.[62]

Epigenetic CRISPR interference (CRISPRi) positive hits verification

2 sgRNA of the top 7 genes (*Trp53*, *Tada3*, *Atm*, *Gemin2*, *Brd9, Snrpa*, *Snrnp48*) and *Cdkn1a* gene were selected for target genes verification (Table S2). With the sgRNA sequence selected, an additional "G" was added to the 5' end of the sgRNA (IDT), and then the sgRNA was inserted into the ipUSEPR lentiviral sgRNA vector with BsmBI enzyme (NEB). Target sgRNA containing lentivirus was produced as previously described. NPC-dCas9-sgRNA cell lines were constructed with lentivirus following the previously described protocol, and then selected with 1 μg/ml puromycin. One cell line of each sgRNA was used for positive hits verification. A new batch of FUCGW-Cre lentivirus was used for target sgRNA verification. 300k NPC-dCas9-sgRNA cells were plated into

one well of pre-coated 24 well plates and allowed to grow overnight. No lentivirus (Mock) or 10 μl Cre-LV (Cre) were added to 200 μl NPC media with 4 μg/ml protamine sulfate for 24 hours. 24 hours after the infection, NPCs were dissociated with 1x TrypLE Express and replated with ~100k NPCs per well to a pre-coated 24-well plate. 120 hours after infection, NPCs were dissociated and counted.

QUANTIFICATION AND STATISTICAL ANALYSIS

We follow standard practices of applying statistical analysis to biological data. Data are presented as mean ± SEM with raw dot plots. Statistical significance was assessed using the standard two-tailed unpaired Student's t test between experimental and control groups. Microsoft Excel (v.14) and Prism (8.0) were used to carry out the aforementioned statistical tests unless otherwise specified. The significance threshold was set as 0.05 and presented as: $p \geq 0.05$, no significant, "n.s."; $p < 0.05$, "*"; $p < 0.01$, "**"; $p < 0.001$, "***"; $p < 0.0001$, "****". Biological replicate numbers "n" and what they represent can be found in figure legends, and "N" in figure legends indicates repeat numbers per biological replicate. Data were blindly analyzed without considering genotypes.